Enhanced Durability of Pt Alloy Nanoparticles Using Sulfur-Doped Graphene via Metal-Support Interactions for PEMFC Cathode Catalysis of ORR

by

Calvin Xu

A thesis

presented to the University Of Waterloo

in fulfilment of the

thesis requirement for the degree of

Master of Applied Science

in

Chemical Engineering

Waterloo, Ontario, Canada, 2017

Author's Declaration

I hereby declare that I am the sole author of this thesis. This is a true copy of the thesis, including any required final revisions, as accepted by my examiners.

I understand that my thesis may be made electronically available to the public.

Abstract

The hydrogen fuel cell is a form of renewable energy generation technology that produces energy electrochemically and can address energy concerns in the near future, especially due to the diminishing supplies of non-renewable fuel sources. However, the major challenge in current hydrogen fuel cells is the slow kinetics of the oxygen reduction reaction (ORR) at the cathode. Current catalysts of Pt/C are not yet cost effective in terms of catalytic activity. In addition, prolonged operation in fuel cell conditions leads to degradation of these catalysts, limiting long-term use. To address this, future fuel cell catalysts must be able to catalyze the ORR more effectively while simultaneously decreasing the content of Pt. The combination of Pt alloys and sulfur-doped graphene is hypothesized to increase both the catalytic activity and durability of the cathode catalyst, thereby increasing the viability of fuel cell technology.

Pt has been alloyed with various other metals to increase catalytic activity, with multimetallic nanoparticles having shown superior performance over pure Pt catalysts. The phenomena responsible for this enhancement have attracted much interest, and proposed models behind the physical as well as electronic mechanisms have been scrutinized. In addition, recent work on sulfur-doped graphene (SG) support materials have been observed to increase the activity and durability of pure Pt catalysts by means of a tethering effect. The combination of Pt alloys with SG have not yet been investigated, and it is not yet known how they will behave in tandem. The interactions on the catalyst active sites will be under the influence of both the support material and the alloy characteristics. Because of this, changes to the physical and electronic structure are typically a convolution of mechanisms from these two components. Literature on Pt alloy catalysts has suggested that Pt combined with late 3d transition metals yield the most active electrocatalysts. In particular, bimetallic Pt-Ni nanoparticles have demonstrated considerable improvements in catalytic activity over state of the art Pt/C catalysts.

In this work, bimetallic Pt-Ni alloy particles are deposited onto SG supports to serve as an ORR catalyst, then subjected to chemical dealloying and post heat treatment steps to produce three electrocatalysts with each representing a different stage of the synthesis procedure. Electrochemical testing of the catalysts will follow guidelines and targets set by the US Department of Energy, while other characterization techniques corroborate physical observations with the electrochemical results. In this project, results showed that the final stage of the prepared catalyst Pt-Ni/SG-PHT exhibited greater stability than commercial Pt/C in ADT conditions of 1500 cycles from 0.05 to 1.3 V vs RHE. The Pt-Ni/SG-PHT catalyst experienced a 27% loss in ECSA from 23.0 m^2/g to 16.7 m^2/g, while Pt/C suffered a 59% loss from 45.3 m^2/g to 18.3 m^2/g. Similarly, the mass activity of the Pt-Ni/SG-PHT catalyst decreased by 28.0% from 93 mA/mg_{Pt} to 67 mA/mg_{Pt}, while that of Pt/C deteriorated by 68.8% from 125 mA/mg_{Pt} to 39 mA/mg_{Pt}.

Acknowledgements

The authors are grateful for financial support provided by the Natural Sciences and Engineering Research Council of Canada (NSERC), the University of Waterloo and the Waterloo Institute for Nanotechnology, as well as TEM imaging provided by the Canadian Center for Electron Microscopy (CCEM).

Table of Contents

List of Figures

List of Tables

Chapter 1 — Introduction

1.1 History of Fuel Cells

A fuel cell is a device which converts chemical energy of a reactant into electrical energy through electrical energy conversion. The fuel cell concept had been effectively demonstrated in the early nineteenth century by Humphry Davy and was followed by pioneering work of scientist Christian Friedrich Schönbein in 1838 on what was to become fuel cells. The term "fuel cell" was first used by Charles Langer in 1889 and with Ludwig Mond, they constructed first practical fuel cell device using industrial coal gas as the fuel and air as oxidant. Despite this, William Grove is generally credited for the invention of fuel cell in 1939. Grove demonstrated that electric current can be produced by placing two platinum strips in separate bottles containing hydrogen and oxygen in the presence of sulfuric acid. However, due to a number of factors including a poor understanding of their principles, unreliable fuel sources, and expensive catalysts, their practical implementation was a challenge at the time. In 1932, Cambridge engineering professor Francis Bacon modified Mond's and Langer's model to develop the first alkaline fuel cell (AFC) but it took until 1959 for Bacon to demonstrate a practical 5 kW fuel cell system. In collaboration with industrial partners, NASA started designing fuel cell generators for manned space missions in the late 1950s and early 1960s. They were first used for the Gemini and Apollo space projects. With this, interest in this technology began in earnest and in recent years polymer electrolyte membrane fuel cells (PEMFCs) for sustainable and clean energy production have drawn dramatic attention as a replacement for fossil fuels.

Diminishing fossil fuel supplies and environmental concerns motivated the development of alternative sources for clean energy. Hydrogen is a potential clean energy source with that has the possibility to replace or minimize dependence on hydrocarbon fuel sources. Hydrogen can be produced from both non-renewable feed stocks and renewable energy sources such as wind, solar,

hydro and biomass. More specifically, hydrogen can be produced by electrolysis of water using electricity generated from renewable sources. Combining these advantages, hydrogen has the potential to develop into efficient energy conversion technologies such as fuel cells.

Two main sources of clean energy are batteries and fuel cells. Both convert chemical energy of fuel and oxidant to electrical energy, with the former being a form of energy storage and the latter being a form of energy generation. Unlike batteries, fuel cells rely on a continuous input of fuel and do not need charging. In fuel cells, only generate electricity, water and heat. In addition, fuel cells have several advantages over thermal combustion engines including high energy conversion efficiency, lack of emissions, and an abundance of fuel. As can be seen, fuel cells are now being considered as a clean power source in areas of transportation as well as in stationary and portable power generation. Combined with other renewable energy sources, this has the possibility of solving potential global energy crises.

While fuel cells have tremendous potential as a clean energy source, one of the major problem associated with this technology is cost. According to the US DOE guidelines, the cost reduction targets are at $40/KW by the end 2020. In consideration of other clean energy technologies such as batteries and supercapacitors, the DOE has set $30/KW as the final cost target. To enable the commercialization of fuel cell on a global scale, fuel cell systems must also have to meet durability targets. Fuel cell system for transportation applications must also compete with internal combustion engines (ICEs) and other technologies. Furthermore, fuel cell systems have to match the lifetime of ICEs in order to be economically viable. In this respect, fuel cells must be operational to 5000 hours of use with less than 10% loss in performance. In comparison to ICEs, this is roughly equivalent of 150 000 miles of driving.

Polymer electrolyte membrane fuel cells (PEMFCs) use hydrogen as fuel, which is oxidized at the anode to form two protons. These are then transported to cathode across a polymer electrolyte where they participate in an oxygen reduction reaction (ORR) to form pure water. Because this product is relatively benign, PEMFC considered as clean energy conversion device. However many challenges associated with PEMFCs including performance, cost and operational durability must be addressed prior to widespread commercialization of PEMFCs.

Researchers have identified several fundamental reasons associated with the degradation and loss in durability for PEMFCs. These include surface area and electrochemical activity loss due to catalyst dissolution, activity loss due support corrosion, catalyst particle growth and agglomeration, voltage loss due to contact resistance between individual components, degradation of the membrane due to chemical and mechanical stress, and a decrease in catalyst and membrane performance due to contamination or poisoning. It is significant to note that out of these major challenges, four of them are associated with the catalyst.

In terms of cost, one of the most expensive components of PEMFCs is the catalyst layer at each electrode; they comprise 55% of the total cost of a PEMFC stack. Platinum nanoparticles dispersed on high surface area carbon black, hereon denoted as Pt/C, are principally responsible for high cost of PEMFC systems. The sluggish kinetics of the oxygen reduction reaction (ORR) at cathode necessitates the use of these expensive Pt/C catalysts. Platinum is currently the best pure metal to catalyze ORR when considering activity and durability. However, reaction mechanisms of the ORR result in energy losses, and these are found in the overpotential and slow kinetics. As a result, the development of new catalysts must be conducted before PEMFCs can be economically feasible.

The volatility and scarcity of platinum has already been identified, and DOE targets indicate a Pt loading of 0.125mg cm^{-2} by 2020. Other relevant DOE targets are shown in table below.

Table 1.1 US Department of Energy Targets for PEMFCs

Characteristics	Units	Targets	
		2011	2020
Power density	W L^{-1}	400	850
Specific power	W kg^{-1}	400	650
Cost	\$ kW^{-1}	49	30
Durability	hours	2500	5000
Pt group metal total loading	mg cm^{-2}-electrode area	0.15	0.125
Mass activity	A mg^{-1} Pt at 0.9 V $_{iR\ free}$	0.24	0.44

1.2 Background on Pt-Based Active Materials

From the well-known volcano plot of ORR activity, [1] it can be seen that the binding energy of oxygen onto a Pt surface is such that pure Pt exhibits the greatest catalytic activity of all elements. The Hammer-Nørskov d-band model asserts that the binding energy of an adsorbate is based on its orbitals' energy levels, those of the d-band orbitals of the material surface, and the subsequent coupling interactions between them. [2] From these factors, the adsorption energy for oxygen will be influenced by any changes in the metal d-band parameters, including its width and the energy of the d-band centre. For ORR catalysis, particular focus has been brought on the d-band centre of the catalyst. The energy of the Pt d-band centre is slightly too close to the Fermi level. [3] At this energy level, oxygen is bound too strongly to the active site compared to the energy that would provide the theoretical maximum activity from the volcano plot, with an approximately 0.1 eV weakening of the binding being optimal. [4] Thus lowering the d-band centre of pure Pt away from

the Fermi level would allow for more balance between oxygen adsorption to desorption and hence more potent ORR electrocatalysis. [5] In addition, the width of d-orbital DOS is closely related to the d-band centre and the effects on the ORR catalysis. From the d-band model, adsorption involves interaction with the catalyst's d-orbitals. The d-band width determines the vacancy of states certain energy levels, as broadening this band causes the lower energy states to be filled. This lowers the average energy of the band, bringing the d-band centre away from the Fermi level. This effect can also be observed in the relationship between the band width and d-band centre as per the rectangular band model. [6]

From this, the most intuitive approach towards increased electrocatalyst activity is to change the d-band centre of the active material so that the oxygen binding energy lies with the proposed maximum. There are several methods by which the d-band centre of a pure metal catalyst have been changed to more favourable energies. Among the most popular of these methods is the combination of Pt with other metals to form metallic alloys, and mechanisms from the resulting metal interaction contribute to an improved catalytic activity. Furthermore, work has been conducted on altering the morphology of Pt catalysts so that the benefits can be obtained from the structure of the electrocatalyst. More focus will be brought on these two fields of study.

1.2.1 Pt Alloy Catalysts

While pure Pt is the most catalytically active element towards the ORR, bimetallic alloys of Pt with other metals have been observed to act as superior catalysts over single elements alone. Alloys with other PGMs, such as Pd or Rh, replace Pt with other elements that are still relatively active towards the ORR so that the second metal does not inhibit the favourable activity of the final Pt-based electrocatalyst. Moreover, the relatively inert characteristics of Pt and other PGMs allow for continued catalyst use in the harsh operating conditions of a PEMFC. For the same reason, other

noble metals such as Au have been attractive for use in bimetallic catalysts. Because of their relatively inert nature and high reduction potentials, membrane contamination by any dissolved metal cations is not as serious a concern for noble metals. [7] Even so, commercial Pt/C itself does exhibit stability issues after continued operation and can still experience dissolution. The use of other metals has been shown to increase the capabilities of an alloyed catalyst beyond that of monometallic Pt catalysts alone. In terms of PGM-based alloys, Solla-Gullón et al. synthesized PtPd nanoparticles via a microemulsion technique while Ye and Crooks demonstrated increased catalytic activity with dendrimer-encapsulated particles of bimetallic PtPd; Alia et al. produced Pt-coated Pd nanotubes via galvanic displacement to reduce the Pt content of their electrocatalyst. [8][9][10] Furthermore, Zhang et al. showed that nanodentrites of alloyed Pt-Ir had bifunctional catalytic capabilities towards the ORR and OER. [11] For non-PGM noble metals, Yeo et al. used Au seeds to form PtAu nanodentrites for greater catalytic activity than Pt/C, whereas Zhang et al. were able to enhance the stability of Pt/C with the use of Au nanoclusters. [12][13] In addition, Liang et al. analyzed nanorods of Pt alloyed with Pd, Ag and Au for catalytic activity and durability experimentally as well as computationally. [14]

While the alternatives listed above are less costly compared to Pt, alloys with yet more abundant elements replace the aforementioned precious metals with vastly less expensive materials. Alloying with transition metals has demonstrated that bimetallic catalysts can exhibit greater catalytic performance than Pt alone. Based on its favourable performance in high-temperature phosphoric acid fuel cells (PAFC), Antolini et al. alloyed V with Pt and revealed alternative reaction mechanisms with the PtV/C catalyst as opposed to commercial Pt/C. [15] After observations as an effective oxidation catalyst at the anode, Xiong et al. synthesized PtW/C for use as a reduction catalyst at the cathode. [16] Greeley et al. identified the early transition metals

Sc and Y as viable elements to alloy with Pt via DFT and demonstrated an improvement in catalytic activity for both bimetallic catalysts in RDE experiments. [17] Moreover, Hernandez-Fernandez et al. investigated PtY catalysts in nanoparticle form, as such alloys had previously only been prepared in other forms. [18] The late 3d transition metals including Fe, Co, Ni and Cu have attracted particular attention and many studies have revolved around alloys with these metals. In fact, the catalytic activity of PtM (where M is Fe, Co, Ni or Cu) bimetallic catalysts has been noted to exceed that of Pt alloyed with precious metals despite the relatively low activity of monometallic 3d transition metals by themselves. [19][20][21][22][23]

In these alloys, the different lattice parameters in the metal constituents induce a contraction or expansion on the lattices of the respective metals. Hence, the lattice constant of Pt can be altered using the lattice constant of the alloyed metal. Changes in the interplanar distance within the metallic lattice have a direct effect on the electronic structure of the material. It has been determined both empirically as well as from simulations that the modifications in the electronic structure from the changing interatomic distance are directly related to the d-band centre of the final active material, with the d-orbital overlap changing with the amount of compressive or tensile strain; in turn, the adsorption energy is dependent on the new d-band energy and hence the adsorption-controlled catalytic activity can be adjusted by the strength of the lattice strain from the alloyed metal. [6] This phenomenon has been referred to as the strain effect. Because of its relationship with lattice changes in the alloyed catalyst, this has also been called the geometric effect. It has been noted that the strain effect can extend numerous atomic layers past the active surface of the catalyst. As a result, various factors including the size and composition of the resulting alloy will have an effect on the catalytic ability of the surface active sites. From these mechanisms it can be seen that the choices in alloying metal, method of alloying, and atomic ratios

of each metal in the alloy are all possible factors that when combined offer a plethora of electrocatalyst alloy types by which the strain effect can be expressed. One such an example would be PtY catalysts binding oxygen intermediates more strongly due to the tensile strain imposed on the Pt component by Y, while the opposite example would be that of compressive strain on Pt weakening the same binding when alloying with transition metals with smaller radii. [18]

A second phenomenon contributing to improved catalysis in Pt alloys is the ligand or electronic effect. Under this mechanism, the electronic interaction between alloyed metals of differing electronegativity result in a short-range charge transfer. It has typically been reported to act across a maximum of a few atomic layers in an alloy catalyst, much fewer than the strain effect. As a more specific example of the ligand effect, the addition of a less electronegative metal to Pt can result in periodic electron transfer events from these new atoms. This transfer has the effect of changing the electronic structure of the catalyst active site; as with the strain effect, the modified electronic structure has a direct relation to the adsorption energy of any relevant species and thus the catalytic activity of the material. Because both the strain effect and ligand effect act in tandem, the electronic structure of an alloy catalyst is typically a convolution of these two phenomena and are usually referenced together in empirical studies.

The ensemble effect is a phenomenon that posits that species of a bimetallic surface must be organized in specific arrangements in order to serve as effective active sites. [24] These configurations of atoms are eponymously referred to as ensembles. Being positioned in this manner allows for a wider range of reaction pathways at these ensembles, some of which may involve more facile sorption mechanisms for intermediates to and from these ensembles. [25][26] As with the aforementioned effects, it is difficult to ascertain the exact contribution that the ensemble effect has on catalysis as it is accompanied by the other effects from alloying. To this

end, studies have been conducted to isolate the extent of the ensemble effect from various atomic arrangements for a number of adsorbates and their associated catalyzed reactions, including but not limited to the ORR. [27][28][29] It should be noted that even for alloys where Pt forms the major constituent, the presence of the second metallic element – or even vacancy in the case of voids or pores – can affect the types and importance of given ensembles. Gan et al. explicitly investigated the nature of nanoporosity and the degradation of such pores in bimetallic Pt-Ni particles to understand the role of porous ensembles for specific activity and catalyst durability in ORR conditions. [30] Research to deconvolute the ensemble effect has been conducted much like the strain and ligand effect; Deng et al. deposited Pt layers onto Au to correlate all three to ORR performance as a function of Pt thickness. [29]

While mostly attributed with the oxidation of alcohol or formic acid fuels at the anode, [31][32] the bifunctional mechanism in Pt-based alloys has also been proposed as a contributing factor towards the enhanced catalysis of the ORR. In this model, the secondary metal is more easily able to facilitate reactions involving intermediates or otherwise promote elementary steps in a reaction scheme that Pt alone cannot. [33] For this reason, this phenomenon has also referred to as the promoted mechanism. [34] The most commonly referenced example of the bifunctional mechanism is that of bimetallic PtRu serving as the anode catalyst for alcohol oxidation, with CO poisons being cleared from active sites by the Ru component in the electrocatalyst. [35] The influence of the bifunctional mechanism has not been as well investigated for the ORR at the cathode, with Pt-based alloy catalysts offering some nominal conjecture towards its importance. [36][37][38] Rather, the majority of reported ORR electrocatalysts with the explicit intent of exploiting this mechanism at the cathode have been Pt-free and/or of relatively esoteric composition. [39][40] Though it may be present for a given alloy, it is believed that the other

effects – particularly the strain and ligand effects – are much more salient for the ORR at the cathode as compared to oxidation reactions at the anode; in fact, catalysis with alloys such as PtAu and PtCu have been shown to be free of the bimetallic mechanism, depending on the morphology of the surface and compositional homogeneity. [41][42]

Based on the fundamental mechanisms listed above, it can be inferred that the composition of an alloyed catalyst will have significant effects on its catalytic activity. Here, the choice of metals to alloy as well as the ratio of the components in the alloy are the major factors that can be optimized. As aforementioned, alloying Pt with the late transition metals Fe, Ni, Co and Cu have produced some of the most catalytically active materials to date. Wang et al. synthesized bimetallic Pt alloys with Fe, Co, or Ni as the secondary metal using carbon black as a support material. With these catalysts, the improvement factor towards specific activity was determined with reference to commercial Pt/C for each. The deliberate homogenization of the particle composition and control over Pt distribution allowed them to conclude that Pt_3Co was the most catalytically active alloy, [43] which concurs with previous findings on bimetallic alloys. [44] Studies on the ideal metal composition for various bimetallic systems have also been conducted. Chen et al. found that for Fe-Pt alloy catalysts, a compositional ratio of $Fe_{42}Pt_{58}$ provided the highest catalytic activity in terms of reaction rate. [45] Similarly for Ni-Pt alloys, Wang et al. optimized the composition and discovered Pt_1Ni_1 was the optimum compared to ratios of Pt_3Ni, $PtNi_2$ and $PtNi_3$. [46]

1.2.2 Size-Controlled Pt Catalysts

The current state-of-the-art catalyst for the ORR at the cathode revolves around Pt nanoparticles deposited onto high surface area carbon black, commonly referred to as Pt/C. The Pt nanoparticles in this commercial catalyst are typically uncontrolled in physical aspects such as size or shape, but are typically spherical particles with a diameter of approximately 2-3 nm. [47]

Intuitively, a reduction in the size of these particles would be assumed to lead to a larger surface area to volume ratio and thus increase the number of active sites for a given amount of Pt. Alternatively, active site number and thus catalytic activity could be maintained with these smaller particles. Unfortunately, it has been observed that further miniaturizing the Pt particle size in current Pt/C catalysts not only yields diminishing returns, but in fact decreases surface area specific activity through a deactivation phenomenon. Work on size-controlled Pt particles has observed that this activity decrease occurs in particles smaller than 2.7 nm in diameter, [48] with larger particles up to 11 nm in size exhibiting an activity improvement; these discoveries have been attributed to a greater number of terraced sites on the surface of larger particles. [49] In addition, the proportion of strongly-binding edge sites to the area of more catalytically facets increases as particle size decreases. At these edge sites, oxygen is bound much more strongly than at other active sites and dissociation is inhibited. Furthermore, it has been determined that the electronic structure of the catalyst changes for extremely small particles possibly due to quantum size effects, and oxygen binding is strengthened for these small particles. [50] It has been deduced by Gasteiger et al. that this size effect will be present both in RDE experiments as well as in MEA testing conditions, as it has been observed in RDE conditions with the non-adsorbing electrolyte $HClO_4$. [51] The effects were verified by Xu et al. for MEAs using size-controlled Pt/C in the range of 3.0-6.5 nm. [52] Otherwise for sufficiently small particles, there is no benefit to decreased size and ORR activity becomes independent of this property. This has been confirmed by various groups such as Yano et al. in the 1-5 nm size regime. [53] Interestingly, ultrasmall particles in the subnanometre regime have been observed to express unexpectedly high activity when prepared as clusters encapsulated by dendrimers. [54] Finally, DFT calculations by Calle-Vallejo et al.

revealed trends in the adsorption energies of oxygen adsorbates for particles in a small enough size regime such that the d-band model was no longer accurate. [55]

Aside from the effects on catalytic activity, stability issues arise from extremely small particles when they eventually degrade from mechanisms such as Pt dissolution, particle aggregation and Ostwald ripening. [18][47] While Pt/C generally catalyzes the ORR under the desired four-electron pathway, Antoine and Durand have demonstrated via RRDE that there is a minor size effect on H_2O_2 generation via the undesirable two-electron pathway in sufficiently small particles. [56] For these reasons, there has been no strong motivation to obtain smaller Pt particles in commercial Pt/C catalysts.

1.2.3 Facet- and Shape-Controlled Pt Catalysts

Based on the differing surface energy of the basal crystal facets for a given metal, it can be inferred that these facets will display different sorption kinetics. For Pt, it was found that the (111) plane has the lowest surface energy and (110) has the highest. In studies involving a non-adsorbing electrolyte such as $HClO_4$, the ORR activity for these facets from highest to lowest is Pt(110) > Pt(111) > Pt(100); in conditions where the electrolyte could poison the active sites with the adsorption of dissociated ions as with the bisulfate ion in H_2SO_4 onto the Pt surface, the order for ORR activity in these facets differ. [57] Wang et al. measured the catalytic activity of 3 nm polyhedra, 5 nm truncated cubes and 7 nm cubes via RDE techniques in H_2SO_4 and attributed the highest activity in the {100} faceted nanocubes to bisulfate adsorption. [58] Komanicky et al. utilized nanofabrication techniques to create Pt arrays with these low-index facets based on appropriately oriented substrates in order to correlate facets and shapes to catalytic activity. [59] From these works, it can be seen that control over the morphology and shape of the Pt catalyst such that more desirable crystal facets become exposed can lead to increases in mass activity.

This is also the case for Pt alloy catalysts, though the most active facet will differ depending on the type and composition of the alloy. In any case, finer control over the shape of the particles allows for investigation into the most active facet of a given electrocatalyst. Work by Stamenkovic et al. on single crystal Pt_3Ni is the most salient example of investigating the catalytic activity for facets of Pt alloy catalysts. It was determined that among the three low-index facets described above, $Pt_3Ni(111)$ was the most catalytically active facet being 10 times more active than single crystal Pt(111) and 90 times more active than commercial Pt/C. [60] This result was further confirmed by Wu et al. using Pt_3Ni truncated octahedra dominated by the $Pt_3Ni(111)$ facet. [61] Similar levels of catalytic enhancement were achieved by Zhang et al. with Pt_3Ni when comparing {111} dominated octahedral to {100} dominated nanocubes. [62] Furthermore, Carpenter et al. synthesized well-faceted Pt alloy nanocrystals using a solvothermal procedure that allowed for shape control; while the procedure was applied to Fe, Co, and Cu precursors, the Pt-Ni catalysts generated the most interest with different facets and morphologies being generated based on the ratio of Pt to Ni. [63] Chen et al. produced hollow Pt_3Ni nanoframes that had several monolayers of Pt on the surface and displayed properties similar to Pt(111) facets after annealing. [64] These nanoframes minimize the amount of unexposed Pt beneath the surface and thereby achieved a high degree of both catalytic enhancement as well as durability over commercial Pt/C. Finally, Choi et al. prepared uniform Pt-Ni octahedra with record mass activity attributable to the surfactant free {111} facets present in their highly controlled synthesis methodology. [65]

The high activity exhibited by the Pt_3Ni has attracted great interest and the works above have been conducted to achieve the most comprehensive understanding of this bimetallic system. However, investigations into the crystal facets of other alloy materials have also been performed. Lee et al. prepared Pt-Pd octahedra with {111} as the dominant facet in differing compositions of

Pt_3Pd_1, Pt_1Pd_1, and Pt_1Pd_3. Electrochemical testing with carbon black as a support revealed that their Octa-Pt_3Pd_1/C catalyst yielded the greatest enhancement in catalytic activity over spherical Pt_3Pd_1/C and the authors attributed this to the high surface area for the {111} facet that was not present in the spherical particles. Nanodentrites with a Pd core and Pt branches were synthesized by Lim et al. and it presented an enhanced mass activity over commercial Pt/C. [66] Such a nanostructure has an intrinsically high surface area, and it was observed that most of the surface was of the {111} facets though {110} and high-index {311} facets were also present.

1.2.4 Pt Monolayers and Core-Shell Structures

The ORR is generally catalyzed by active sites on the surface of an electrocatalyst. Subsurface atoms may indirectly affect the reaction through mechanisms described above, but do not directly contribute in the form of active sites. As a result, work has progressed towards core-shell morphologies or thin Pt layers deposited over other materials with the motivation of decreasing the precious metal loading in the final electrocatalyst and thus increasing the commercial feasibility of Pt-based catalysts. Core-shell structures are usually associated with alloy catalysts, with the Pt forming the shell of the particle and the non-noble metal forming the core. The most direct means of achieving a core-shell structure is a single step impregnation reduction methodology as conducted by Wang et al. to produce Pt_3Co@Pt core-shell nanoparticles. [67]

Otherwise, a core-shell particle can be prepared using a number of different procedures. One method begins with a particle of Pt alloyed with a transition metal. A selective dissolution procedure consisting of sustained acid exposure will cause transition metals at the surface to become oxidized. This acid leaching of the particle leaves vacancies which then causes diffusing Pt atoms to enrich the surface. [68] The diffusion phenomenon leaves many defects at the surface, and literature denotes these types of core-shell particles as Pt skeleton structures. [44] This

approach was conducted by Wang et al. to produce Pt skeleton structures from Pt-Ni alloy nanoparticles. [46]

An alternative approach involves the induced segregation of Pt atoms to the surface of the particles. This can be done by heat treating an alloy particle. This thermal annealing restructures the surface of the nanoparticle so that a pure Pt monolayer is formed around the bulk of the particle. At the same time, the Pt content of the immediate subsurface layer has been observed to decrease indicating a thermally-induced segregation phenomenon. [44] This type of core-shell structure has been referred to as a Pt-skin surface in literature. The exact mechanisms for segregation processes are not known for each alloy configuration, but it is possible to conduct Monte Carlo simulations to determine the relationship between annealing parameters and the final segregated particle. [69] One example of this procedure is a comparison of Pt-skin and Pt-skeleton core-shell structures in work performed by Stamenkovic et al. on Pt alloyed with various transition metals. [70] The disadvantage of this method is that annealing can lead to a decrease in the electrochemically active surface area and the growth of metal particles by sintering and similar phenomena. [69]

A third method of creating core-shell structures involves the deposition of Pt monolayers over a core of another material. In a colloidal synthesis procedure, Pt monolayers form on nuclei of other materials. The exact mechanisms behind this colloidal nucleation will depend on the seed material, with many parameters affecting the growth mode and crystallinity of the final core-shell particle. Such a technique allows for monodisperse particles to be produced with a fine control over the Pt shell thickness. [69] However, it is extremely dependent on the seed material as the associated growth mode may not yield monolayer Pt on the surface. Wang and Toshima implemented a colloidal synthesis to produce Pd@Pt core-shell particles in the size regime of 1.5-5.5 nm. [71]

1.3 Background on Support Materials

It has been established that the inclusion of a support material enhances the activity and stability of an electrocatalyst over metal particles alone. [72] For state of the art Pt/C catalysts, the support material is typically in the form of carbon black. These carbon blacks are small enough to be considered 0-dimensional supports. Regardless of the manufacturer, they can be considered electrically conductive, have high surface area and are readily available in large supplies. Along these properties, literature has identified key properties of an ideal support material, including high electronic conductivity, corrosion resistance, uniformity in size and shape, high surface area, strong binding with metallic catalyst particles, and dispersed nucleation sites for catalyst precursors, [73] as well as strong metal-support interaction, porosity to maximize the triple-phase boundary, and flooding resistance. [74] While carbon blacks are relatively cost-effective support materials that address some of these criteria, increasing demands in electrocatalyst capabilities mean that an optimal support would confer benefits beyond the inherent limitations of carbon blacks.

One of the primary motivations in developing novel support materials involves durability concerns with carbon black. At higher operating potentials, carbon corrosion becomes a serious issue. While Pt does become macroscopically oxidized at these potentials, it merely becomes passivated by an oxide film which can be reduced at lower potentials to recover the Pt surface. It should be noted that this is the dominating cause of immediate catalytic inhibition Pt particles, with more drastic mechanisms such as sintering and agglomeration being more noticeable over prolonged operation. Unfortunately for carbon black, corrosion at high potentials permanently affects the performance of the electrocatalyst as attached metal particles become lost due to breakoff of the support material. The second primary impetus towards support material research

revolves around the observed enhancement of the capabilities of the catalyst in terms of catalytic activity. As aforementioned, researchers have determined that the choice of support material plays as significant a role in electrocatalyst performance as the characteristics of the active material particles. [73] From here, novel support materials for Pt catalysts attempt to address these criteria of durability and activity enhancement. While the intent is to pursue both simultaneously, the general trend is for non-carbonaceous support materials to target stability and for carbonaceous support materials to focus on catalytic improvements. As always, there are exceptions to this and the effects of each category will be briefly discussed.

1.3.1 Non-Carbonaceous Support Materials

One subcategory of non-carbonaceous support materials is that of conducting metal oxides. Unlike carbon black, carbon corrosion does not affect metal oxide materials which are essentially inert in fuel cell operating conditions. Many electrochemical studies have been conducted on the viability of oxides such as titanium oxide, tin oxide, silicon dioxide and tungsten oxide. It was noted that titania exhibited excellent corrosion regardless of the acid used as the electrolyte. [74] In addition, electrical conductivity was comparable to that of graphitic materials. Durability tests with tin oxide by Masao et al. revealed similar stability characteristics, even after 10 000 cycles with an upper potential of 1.3 V vs RHE. [75] Seger et al. deposited Pt particles on silicon dioxide as a support material for fuel cell testing in MEA conditions and found that the optimum composition provided a power density comparable to that of Pt/C; [76] unfortunately, poor electrical conductivity severely limits the viability of silicon dioxide as a support material. Tungsten oxide demonstrates similar stability behaviour as other metal oxide support materials even in acidic conditions and in elevated temperatures, [77] though a non-negligible level of tungsten dissolution in acid is still present.

A second subcategory of support materials is that of transition metal carbides (TMCs). Due to cost concerns with the use of Pt catalysts, TMCs have also been employed as catalytic active materials by themselves, though further details of pure TMC electrocatalysts are beyond the scope of this work. Among TMCs, tungsten carbide has received particular attention as its electronic structure resembles that of pure Pt near the Fermi level. [78] As a support material, improvements over commercial Pt/C have been attributed to a synergistic effect between the metal and support. [79] When acting as a support material for Pt particles in MEA form, it also displayed resistance to the oxidizing conditions of PEMFC operation by retaining greater catalytic activity compared to commercial Pt/C. [80]

1.3.2 Carbonaceous Support Materials

Novel carbon-based support materials have been developed in order to circumvent the limitations brought about by carbon blacks. Among the most popular carbonaceous alternatives are carbon nanotubes (CNTs), which can be considered 1D support materials to the nearly 0D carbon blacks. Its appeal is brought about by advantageous characteristics including high surface area, electronic conductivity and chemical stability. [81] Unfortunately, bare CNTs are typically inert and lack the appropriate binding sites upon which metal particles can attach. As such, CNTs are usually functionalized via acid treatment before serving as support materials. Otherwise, less than 30wt% loading of Pt can be conducted on multi-wall CNTs (MWCNTs). The electrochemical stability of Pt loaded onto MWCNTs was demonstrated by Park et al., with this new catalyst suffering from a smaller degradation in performance as compared to Pt loaded onto Vulcan XC-72 carbon black. [82] Unfortunately, the lack of a high scale methodology currently prevents CNTs from being available as a support material in commercial catalysts.

Graphene can be considered the 2D analogue of 1D CNTs and nearly-0D carbon blacks, and interestingly addresses many of the characteristics of an effective support. Boasting large surface area as well as one of the highest electron transfer rates and high conductivity, graphene has already established itself as a popular support material for electrocatalysts. In particular, the fast electron transport in graphene is hypothesized to more easily facilitate the ORR. Deposition of metallic materials onto the basal planes of graphene can be relatively difficult despite its large surface area. On the other hand, these basal planes can resist oxidative attack and corrosion much more easily than carbon black. [83] One challenge associated with graphene-based materials is that of graphene sheet restacking via strong π-π interactions; this leads to mass transport concerns as oxygen can no longer reach sheets in the middle of a stack, and any generated water can result in flooding of the electrocatalyst if there is difficulty in water removal. In any case, studies on the capabilities of graphene have been conducted both in RDE and in MEA methodologies.

1.3.3 Doping of Support Materials

The inclusion of various elements to a support material allows for tailored characteristics to either enhance desirable characteristics or to mitigate the deficiencies in a given support material. In the context of metal oxide materials, electrical conductivity can be increased by the addition of certain dopants. Park and Seol recognized the conductivity bottleneck in TiO_2 and doped the support with Nb. [84] Haas et al. doped a TiO_2 support material with Ru based on the requirement that greater than 27 mol% of Ru would provide sufficient conductivity. [85] More drastic conductivity issues with SnO_2 encouraged the use of dopants to increase the overall performance of this metal oxide; Lee et al. used Sb as a dopant for SnO_2 to increase the conductivity of the support material to 0.11 S/cm. [86] Interestingly, Chhina et al. reported high stability with TiO_2 support materials doped with Nb after subjecting the electrocatalyst to a potential of 1.4 V for 60

h. [87] Huang et al. had similar durability observations after potential cycling Nb-doped TiO_2 in MEA conditions. [88]

Carbonaceous support materials have also been subject to doping to enhance their capabilities. Nitrogen has been especially ubiquitous as a dopant in many carbon-based support materials, and has been of particular focus for non-Pt based electrocatalysts. That being said, other elements have been utilized as dopants including boron, [89] fluorine, [90] and phosphorus. [91] In any case, several major benefits have been identified in doping graphene-based materials. [92] Firstly, such dopants provide nucleation sites without the need for functionalization techniques. Secondly, introducing dopants into a graphene-based structure can modify the electronic structure any deposited Pt particles, enhancing the catalytic capabilities of the electrocatalyst. Lastly, metal-support interactions can be strengthened to anchor Pt particles to the support material and mitigate degradation mechanisms. [83] Such work has been conducted with nitrogen and activated graphene by Choi et al., [93] with the nitrogen dopant assisting in the dispersion of deposited Pt particles, enhancing the ORR activity and stabilizing the electrocatalyst; electrochemical testing in RDE conditions revealed these effects, with potential cycling for 1000 cycles in N_2 saturated electrolyte serving as an accelerated durability test (ADT).

While not as popular as nitrogen, sulfur has become an increasingly utilized dopant for carbonaceous supports. Preliminary studies on sulfur-doped graphene (SG) by Higgins et al. revealed an enhancement in catalytic activity towards the ORR over commercial Pt/C with a mass activity of 139 mA mg_{Pt}^{-1} compared to 121 mA mg_{Pt}^{-1} at 0.9 V vs RHE. [94] Furthermore, there was an 87% retention in the ECSA of SG and decreased loss in mass activity compared to Pt/C, with 108 mA mg_{Pt}^{-1} for the former and 39.8 mA mg_{Pt}^{-1} for the latter at 0.9 V vs RHE. Similar

results were achieved for Pt nanowires supported by SG. [95][96] From this, it can be seen that sulfur has much potential as a dopant for support materials.

1.4 Scope and Motivation for Current Work

Unlike nitrogen-doped supports, sulfur as a dopant for support materials has not yet been fully investigated. Previous studies on sulfur-doped graphene as outlined above have provided promising results towards catalyzing the ORR at the cathode. As discussed in the references above, interactions between the metal particles and support can be described as a "tethering" phenomenon that can enhance the longevity of the catalyst under continued PEMFC operation. However, the reported works have been conducted with monometallic Pt. As per *1.2.1 Pt Alloy Catalysts*, the constituents of multimetallic catalytic particles exert various phenomena upon each other which can affect both the physical and electronic structures of the final electrocatalyst. Combining this with the metal-support interactions between a sulfur-doped support material and the Pt alloy particle, it can be inferred that the mechanisms from doping and alloying will both impose a convolution of effects on the final material. As a result, current work encourages the investigation of sulfur-doped support materials in the presence of alloyed active materials. This will be discussed in *Chapter 3*.

Chapter 2 — Characterization Methods

2.1 Physical Characterization

2.1.1 Electron Microscopy

Electron microscopy is an imaging technique that utilizes electrons rather than photons as in conventional microscopy. The capabilities of optical microscopy are limited by certain phenomena and quantitative metrics such as image resolution are controlled by physical parameters. More specifically, the minimum feature size that can be resolved by a beam can be given by the resolution R in the following relationship:

$$R = 0.61\frac{\lambda}{NA} \qquad \text{(Equation 2.1)}$$

where λ is the wavelength of the beam and NA is the numerical aperture of the system. The numerical aperture can be increased by design elements such as oil immersion, but the most salient limitations are related to the wavelength of light; light in the visible spectrum thus restricts what wavelengths can be used, and with the minimum wavelength yields an approximate resolution of 200 nm under the most ideal design conditions. This is insufficient to image the materials produced in this work, where particles can be as small as several nanometres in diameter.

In comparison, an electron acting as a matter wave exhibits much more favourable characteristics towards imaging. The energy of the electron matter wave is given by

$$E = \frac{h^2}{2m_e\lambda^2} \qquad \text{(Equation 2.2)}$$

where h is Planck's constant, m_e is the mass of the electron, and λ is the electron's de Broglie wavelength. For a typical accelerating voltage of 10 kV (for an electron energy of 10 keV) and a numerical aperture of 0.01, the wavelength is found to be 0.12 Å. As can be seen, much smaller resolutions can be achieved via electron microscopy. Because these electrons are so energetic, the

chamber of an electron microscope must be placed under ultra-high vacuum to prevent the high-energy electrons from interacting with free gas molecules instead of the sample.

It can be noted from above that the resolution is dependent on the electron energy and accelerating voltage, which is in turn related to the electron gun used in the microscope. Electron guns with a tungsten or LaB_6 filament produce electrons through thermionic emission, whereby thermal excitation through the filament provides enough energy for electrons to overcome the material's work function to escape into free space. Similarly, other guns operate by field emission which is a quantum mechanical tunneling process that does not require heat and produces electrons with a narrower energy distribution. These electrons are focused in a Wehnelt cylinder inside the electron microscope and controlled by electromagnetic lenses to the specimen. From here, the specimen choice as well as the method of collecting the electrons differ in transmission and scanning electron microscopy.

In this study, both scanning and transmission electron microscopy have been conducted to image the materials to qualitatively determine the physical properties relevant to the electrocatalysis of the ORR. Such investigations will be discussed in more detail in sections *2.1.1A* and *2.1.1B* below.

2.1.1A Transmission Electron Microscopy

In transmission electron microscopy (TEM), the electrons pass through the specimen and then typically through projector lenses to be displayed in a multi-step magnification process. Because the electrons must penetrate the specimen, samples too thick to allow any electrons to travel through cannot produce an image. The electron path changes after interaction with the sample, with these interactions changing the intensity of collected electrons for the image. As such, an image is formed based on the atomic characteristics as well as thickness of the specimen being

imaged. A further application of TEM is mass density contrast, whereby contrast in the image is taken from the intensity as compared to the average atomic number Z; it should be noted however that any detected contrasts in mass density resulting from these interactions is primarily due to electron scattering, not absorption. An additional contrast formation technique is diffraction contrast, in which crystal facets preferentially scatter the electron beam depending on the degree by which the sample stage is tilted.

In order to image with this technique, the sample is drop-casted onto a TEM grid made of copper coated with amorphous carbon. Within the microscope chamber, electrons emitted from the gun interact with the sample on the grid and are collected with as described above. With this technique, the electrocatalysts in this work can be imaged for the qualitative study of the physical metal-support interaction, such as the size and level of dispersion of the metal particles on the support material.

More specifically for this work, TEM was performed to image the electrocatalysts before and after being subjected to electrochemical testing. Observations made from the beginning of life (BOL) state as compared to the end of life (EOL) state allowed for analysis of degradation mechanisms hypothesized for typical cathode catalysts, such as corrosion of the graphene support material and growth of the catalytically active particles by phenomena including Ostwald ripening and sintering. Such changes in the catalysts from the BOL to the EOL states can then be associated with qualitative data collected during electrochemical testing, such as active surface area and the catalytic activity.

2.1.1B Scanning Electron Microscopy

Scanning electron microscopy (SEM) utilizes secondary electrons (SE) and backscattered electrons (BSE) produced in the sample by the incident electron beam from the electron gun. The

depth from which SEs and BSEs can be produced is dependent on the energy of the initial electrons, but because the sample itself can prevent deep electrons from being released the maximum depth that electrons can be collected is generally 300 nm. From this, it can be seen that SEM is considered a surface characterization technique. Surface charging from electron accumulation is a concern for non-conductive materials, necessitating the use of sputtering prior to SEM imaging. The energy of the SE and especially BSE will depend on the atomic composition of the sample, allowing for the discrimination of material composition. In addition, intensity and brightness can be affected by crystal orientations, allowing for facets to be detected.

SEM can show the highly conductive metal particles deposited on the support material. To perform this microscopy, electrocatalyst powders are deposited onto double-sided conductive carbon tape affixed to SEM stubs. In similar function to TEM, the size and dispersity of these particles on the support can be determined. Furthermore, X-rays produced from the incident beam can be collected in an additional characterization technique described below in order to determine the surface elemental composition.

For this work, SEM allows for a facile alternative to TEM when imaging the electrocatalyst surface. From images at various levels of magnification, the quality of the electrocatalyst can be estimated based on factors such as the size and distribution of the alloy metal particles deposited on the surface of the graphene support. The appearance of large particles is an indicator of a low surface area to volume ratio and thus fewer active sites available for the ORR, whereas a poor distribution of particles on the graphene sheet tends to imply a poor activity due to transport issues to and from the active sites.

2.1.2 Energy-Dispersive X-Ray Spectroscopy

When incident electrons eject core electrons from atoms in a sample, electrons from the higher energy valence shell take their place. This relaxation produces X-rays that can be collected by an electron microscope in a technique referred to as energy-dispersive X-ray spectroscopy (EDX). Because this based on a relaxation phenomenon, the energy of these X-rays will be characteristic of the element involved and allows for such elements to be identified. On the other hand, the presence of many elements with similar characteristic X-rays can prevent each element from being uniquely determined.

For this study, EDX was performed to verify the presence of the alloy metal particles on the prepared electrocatalysts as well as that of the sulfur dopant in the graphene support. Additionally, elemental mapping of the catalyst via EDX displayed the distribution of each element on the support material for each of the studied catalysts. As a result, these elements could be confirmed by both mapping and the spectra obtained by EDX. Furthermore, the use of mapping would determine if the particles found in microscopy were alloyed particles or pure metal particles alone.

2.1.3 X-Ray Diffraction

X-ray diffraction (XRD) is a characterization technique that uses an electron gun to produce high-energy incident electrons which knock out core electrons from a crystalline sample, generating characteristic X-rays in the resulting relaxation process. Because the electron gun typically operates by thermionic emission, a form of cooling is required with the system. The angle between the electron gun and X-ray detector is controlled by a goniometer, allowing for the intensity of detected X-rays to be controlled with respect to the angle. For a crystalline sample, a signal peak is only obtained when the path difference between sets of planes with an interplanar distance d_{hkl} is such that constructive interference occurs according to Bragg's law:

$$2d_{hkl} \sin\theta = \lambda \quad \text{(Equation 2.3)}$$

where θ is half the angle between the electron gun and X-ray detector and λ is the wavelength of the beam, and these parameters are correlated such that the aforementioned constructive interference is possible.

In this study, XRD spectra of the prepared electrocatalysts were collected and compared to the spectra of Pt and Ni to confirm the successful syntheses of the catalysts. Moreover, the relative intensity of the XRD peaks corresponding to the different Pt crystal facets would correlate to the results of electrochemical testing as certain facets have greater catalytic activity towards the ORR than others.

2.1.4 X-Ray Photoelectron Spectroscopy

In X-ray photoelectron spectroscopy (XPS), photons from an X-ray source energetically emit an electron in the sample via photoelectric excitation. The kinetic energy E_K of the electron upon being detected can be based on the energy of the X-ray source as well as the material as per

$$E_K = h\nu - E_B - \phi \quad \text{(Equation 2.4)}$$

where E_B is the binding energy of the atom in the material and ϕ is an energy cost for the electron to reach the detector, affected by variables such as work function and sample-detector potential difference. Despite the high penetration of the photons, the resulting photoelectrons have a relatively low energy and cannot escape from deep within the sample. As such, XPS is considered a surface characterization technique.

XPS is employed in this work to obtain the elemental concentrations of mainly platinum and nickel for the particles deposited onto the support material. In addition, shifts in the peaks of the XPS spectra indicate an interaction between the platinum in the particles with the alloyed nickel as well as with the sulfur dopant in the graphene support.

2.1.5 Inductively Coupled Plasma Spectroscopy

As the name implies, inductively coupled plasma (ICP) spectroscopy is a characterization technique that utilizes plasma generation in a chamber surrounded by an induction coil with the intention of analyzing the elemental composition of a material sample. The generated plasma bombards the specimen, energizing and ionizing the atoms of the material. These high energy excited states are short-lived and must relax to a more stable ground state. Upon relaxation from the excited states, radiation will be emitted with wavelengths characteristic of the elements involved in the analyte. Coupling ICP with atomic emission spectroscopy (AES), the combined characterization technique ICP-AES uses a photodetector to determine the intensity distribution of the radiation across a range of wavelengths.

In order to conduct ICP-AES in this work involving Pt catalytic materials, the material is first subjected to digestion in appropriate acids such as aqua regia. This is done to ensure homogeneity within the specimen in order to determine the bulk composition; because ICP-AES is a surface-sensitive process, leaving the electrocatalyst in solid form would show only the exposed elements and would be affected by nanostructures including core-shell morphologies. Once the digested solution of catalyst is in the spectrometer chamber, plasma is generated and induction coils focus the bombardment onto the sample. The radiation from the relaxation of excited states is then collected by photodetectors, with photomultipliers implemented to amplify the signal from the received wavelengths.

For this work, ICP is performed in order to determine the ratios of Pt to Ni in the alloy metal particles, which is then used to find the precious metal loading of the electrocatalyst and thus the Pt mass normalized activity.

2.2 Electrochemical Characterization

The true capabilities of a fuel cell electrocatalyst under realistic conditions are only fully known when it is used in a proper fuel cell stack, with many parameters such as gas exchange into the catalyst layer or susceptibility to flooding only being present in such a set-up. As such, electrochemical testing in a fuel cell station is considered to provide the most authoritative data for a fuel cell catalyst. Unfortunately, such testing requires a relatively large amount of catalytic material to be coated onto a complete membrane-electrode assembly (MEA) consisting of a Nafion membrane as well as gas diffusion electrode (GDE) and gas diffusion electrode (GDL). In addition, the preparation of a complete MEA requires a significant amount of time and attention. For these reasons, the fuel cell station is a relatively cumbersome electrochemical testing method.

In comparison, a rotating disk electrode (RDE) in a half-cell setup can determine the electrocatalytic capabilities of a material with significantly decreased resources and time. This test can be considered to be the idealized performance of the catalyst as many more subtle phenomena are not present as with the MEA in a fuel cell stack. As a result, the catalytic activity under half-cell conditions are reported independently of those under fuel cell conditions. Furthermore, fuel cell catalyst targets set by the DoE discriminate between the two. Despite these differences, catalyst testing under half-cell conditions is still the standard and ubiquitous technique due to its ease.

In the half-cell setup, the RDE cell uses three electrodes and a potentiostat to control the system. The reference electrode (RE) provides a known standard by which the other two electrodes can be compared. There is a number commercially available of reference electrodes, with selection dependent on the testing conditions. As an example the Ag/AgCl electrode is a common reference electrode in alkali conditions while in this work with Pt catalysis towards the ORR, the reversible hydrogen electrode electrode (RHE) is typical. The counter electrode (CE) represents the anode of

the fuel cell and is usually Pt, commonly taking the form of a wire or mesh to maximize surface area. The electrocatalyst of interest is deposited on the glassy carbon (GC) of the working electrode (WE). The electrodes are inserted into the RDE cell and immersed in an appropriate electrolyte. For ORR catalysis with Pt, $HClO_4$ is normally used as its anion exhibits less adsorption to catalytic active sites than those of other acids.

Prior to testing, the electrolyte is purged with either N_2 or O_2 gas until saturated. The choice of saturated gas depends on the electrochemical test that is to be done. In this work, the two main electrochemical characterization techniques involve the cyclic voltammogram and ORR polarization curve of the catalyst. Because the catalytic capabilities of a material can degrade under continued operation, these two can be again obtained following a degradation test.

2.2.1 Cyclic Voltammetry

In cyclic voltammetry (CV) of a Pt-based catalyst, electrocatalytic parameters such as the electrocatalytically active surface area (ECSA) can be determined from the catalyst when immersed in N_2-saturated electrolyte. Such an area indicates the number of catalytic active sites present in the material, with a larger ECSA generally increasing catalytic activity by providing a greater number of sites for the ORR to take place. The ECSA is determined from peaks in the CV corresponding to hydrogen adsorption/desorption from the Pt catalyst surface.

In this work, the ECSA was calculated in m^2/g using the integral of the hydrogen desorption peak as per the following relation:

$$\text{ECSA} = \frac{Q/r}{\Gamma \times L \times A} \qquad \text{(Equation 2.5)}$$

where Q, in Coulombs, corresponds to the charge integrated from the hydrogen desorption peak from the anodic sweep; r is the scan rate in mV/s, $\Gamma = 210\ \mu C/cm^2$ is the charge required to

reduce a hydrogen monolayer from a polycrystalline Pt surface; L is the Pt loading onto the glassy carbon working electrode, here taken to be $20\ \mu g/cm^2$; and A is the area of the glassy carbon electrode in cm^2. [97]–[100] Accelerated degradation testing (ADT) was conducted in similar conditions, with 1500 cycles from 0.05 to 1.3 V vs RHE instead. The CV of each catalyst was obtained pre- and post-ADT. Pre- and post-ADT ORR polarization curves were obtained from the anodic scan from 0.05 to 1.2 V vs RHE at 5 mV/s in O_2-saturation.

2.2.2 ORR Polarization

The ORR polarization curve provides the actual catalytic activity of the catalyst. Conducted in O_2-saturated electrolyte, rotation of the WE induces laminar fluid flow directly into the catalyst-deposited GC. This flow carries the dissolved oxygen gas into the catalytic active sites, and increasing the rotation rate increases the amount of oxidant flowing into the catalyst. Hence the limiting current, defined as the maximum current at which further potential changes will not increase the current as all diffused oxygen is already reacted, can be increased by increasing the rotation rate. In this work, ORR polarization curves were typically conducted at a rotation rate of 1600 rpm.

The measured current i, taken from the polarization curve, is a combination of the kinetic current i_k and the diffusion-limited current i_d. The diffusion-limited current itself is dependent on the rotation rate of the RDE according to the Levich equation below:

$$i_d = 0.620nFAD^{\frac{2}{3}}\omega^{\frac{1}{2}}\nu^{-\frac{1}{6}}C \qquad \text{(Equation 2.6)}$$

where n is the average number of electrons transferred in the reaction, F is Faraday's constant, A is the area of the electrode, D is the diffusivity of the reactant, ω is the rate of rotation, ν is the electrolyte kinematic velocity, and C is the concentration of dissolved oxygen. Because i_d has a

dependence on rotation rate, the kinetic current i_k is of interest in determining the inherent catalytic ability of a material.

In this study, ORR polarization curve is obtained in order to determine the currents in the regimes mentioned above. With these currents, the catalytic activity of the electrocatalysts at the DOE standard potential of 0.9 V vs RHE can be calculated.

Chapter 3 — Stabilization of platinum-nickel alloy nanoparticles with sulfur-doped graphene support in polymer electrolyte membrane fuel cells

3.1 Introduction

Continued use of non-renewable fossil fuels is becoming more economically and environmentally unsustainable, leading to an unmet demand for alternative sources of energy generation. Among these new sources, polymer electrolyte membrane fuel cells facilitated by platinum-group metal catalyzing the oxygen reduction reaction (ORR) at the cathode have attracted much interest as a green power technology. In turn, the practicality of such fuel cells is limited by the scarcity of platinum and the loss of output power after degradation from continued use. Motivated by the high costs of these catalysts, a reduced noble metal loading has been made possible by compensating with high activity electrocatalysts. Approaches to increase catalytic activity include alloying Pt with transition metals and supporting the metal with stable carbon nanomaterials such as carbon nanotubes [101] or graphene. [83][105] It has been reported that the lattice-strain phenomenon is the primary mechanism [22][103]–[105] by which platinum alloys can achieve greater catalytic activity over platinum alone. Oxygen binds too strongly to pure platinum due to the latter's d-band electron energy levels [1] but by inducing a strain on the surface through metal alloying, the electronic structure of the surface can be shifted so that oxygen species are bound more weakly, allowing adsorbed OH to more easily dissociate and free the active site. [5] This has been shown with transition metals such as iron, [106]–[108] copper, [109] and cobalt [21][110]–[113] as well as with noble metals in nanostructure morphologies. [114]–[118] In particular, nickel-based alloys have shown levels of catalytic activity greater than those based on other transition metals. [23][60][65][119]–[121]

Unfortunately, there are major challenges with transition metal dissolution under acidic conditions due to the low dissolution potentials of such elements. In addition, other concerns with the stability of PEMFC catalysts involve the degradation of the support material, which is typically carbon black. This results in either the breakoff of attached metal particles from the support or the direct corrosion of the carbon itself, both of which are exacerbated at upper operating potentials. As this is the result of weak interaction between the support and active material, dissolution and support instability can be solved through enhanced bonding between the electrocatalyst components. Nanocarbon support materials such as graphene have become increasingly popular as the main focus of catalytic research in recent years. Furthermore, doping graphene with elements such as nitrogen,[93] phosphorus and boron has yielded improved catalytic performance. [122]–[124] In particular, recent developments involving sulfur have yielded impressive platinum-based catalysts. [95][96][125] This doping technique has further been observed to improve the longevity of the catalyst,[94] and this is posited as due to the strengthened metal-support bond preventing the breakoff of the metal species. [92] As such, the incorporation of sulfur-doped graphene (SG) as in this work would show great promise for improving the activity and stability of Pt alloy catalysts.

Previously, our group had reported the use of SG to support platinum nanoparticles and nanowires with the effect of increased activity and stability, with density functional theory (DFT) modelling corroborating these results. [94][96][124] In these simulations, it was determined that pure platinum deposited onto sulfur-doped graphene (Pt/SG) had an adsorption energy of -2.68 eV versus -2.01 eV for pure platinum on graphene (Pt/G), a d-band centre at -2.72 eV for Pt/SG versus -2.33 eV for Pt/G, and a cohesive energy of –3.95 eV for Pt/SG versus -3.67 eV for Pt/G. However, the synergistic behaviour between SG and alloyed platinum has yet to be investigated. The changes

in electronic structure introduced into a Pt alloy by the lattice-strain from a transition metal such as nickel can have very drastic effects on the binding strengths of sulfur dopants as compared to pure Pt, and the impact on both catalytic activity as well as stability must be considered. Herein, we report the performance of a platinum-nickel catalyst supported by SG, here referred to as Pt-Ni/SG, and the role of SG for bimetallic Pt-Ni. The synthesis of the alloy was conducted using the well-established polyol method as found in literature, then the catalyst was chemically dealloyed for Pt-Ni/SG-DA and finally subjected to thermal annealing for Pt-Ni/SG-PHT. Electrochemical testing was performed on the alloy, dealloyed and heat treated catalysts with physical characterization used to correlate the behaviour with the catalyst morphology with the final as-prepared catalyst Pt-Ni/SG-PHT demonstrating excellent stability as compared to commercial Pt/C.

3.2 Experimental

3.2.1 Physico-chemical Characterization

Samples were imaged by transmission electron microscope (TEM, JEOL 2010F). Characterization was also conducted through x-ray diffraction (XRD, Rigaku Miniflex), and inductively coupled plasma spectroscopy (ICP, Teledyne Leeman Labs Prodigy High Dispersion ICP system).

3.2.2 Electrochemical Measurements

For electrochemical testing, a five-neck glass cell for rotating electrodes was filled with 200 mL 0.1 M $HClO_4$, with a Pt wire as the counter-electrode and a reversible hydrogen electrode (RHE) as the reference electrode. A 0.196 cm^2 glassy carbon working electrode was cleaned and polished thoroughly prior to deposition with 10 μL of catalyst ink (2 mg of catalyst dispersed in 990 μL of 1-propanol and 10 μL of 5wt% Nafion® solution). All working electrodes were prepared

with a Pt loading of 20 μg/cm^2, and the ink composition of the commercial Pt/C (TKK, 28wt% Pt) used in comparison was modified accordingly. Each catalyst was electrochemically activated in N_2-saturation by cycling from 0.05 to 1.3 V vs RHE at a scan rate of 50 mV/s for 30 cycles to obtain the steady-state cyclic voltammogram (CV) curve. The electrochemical surface area (ECSA), in m^2/g, was determined via (Equation 2.5)(Equation 2.1):

$$\text{ECSA} = \frac{Q/r}{\Gamma \times L \times A}$$

where Q, in Coulombs, corresponds to the charge integrated from the hydrogen desorption peak from the anodic sweep; r is the scan rate in mV/s, $\Gamma = 210\ \mu\text{C/cm}^2$ is the charge required to reduce a hydrogen monolayer from a polycrystalline Pt surface; L is the Pt loading onto the glassy carbon working electrode, here taken to be $20\ \mu\text{g/cm}^2$; and A is the area of the glassy carbon electrode in cm^2. [97]–[100] Accelerated degradation testing (ADT) was conducted in similar conditions, with 1500 cycles from 0.05 to 1.3 V vs RHE instead. The CV of each catalyst was obtained pre- and post-ADT. Pre- and post-ADT ORR polarization curves were obtained from the anodic scan from 0.05 to 1.2 V vs RHE at 5 mV/s in O_2-saturation.

3.2.3 Graphene Oxide (GO) Synthesis

Graphite was oxidized via an improved Hummer's method to yield GO as described in literature. [96] Briefly, 2 g of graphite powder (Alfa Aesar, natural, microcrystal grade, APS 2-15 micron, 99.9995%) was added to a mixture of concentrated H_2SO_4/H_3PO_4 (360:40 mL) in an Erlenmeyer flask and stirred for 30 minutes. 18 g of $KMnO_4$ was then added very slowly to the mixture, and the flask was heated to 50°C for 16 hours. After heating, the flask was cooled to approximately 10°C in an ice bath and 400 mL of DDI H_2O was added to the mixture dropwise.

Finally, 15 mL of H_2O_2 (30%) was added to the mixture. The mixture was centrifuged and washed with water, ethanol and HCl (30%), and then freeze dried for 3-4 days.

3.2.4 Sulfur-Doped Graphene (SG) Synthesis

GO was mixed with phenyl disulfide (99%, Sigma-Aldrich) in a 2:1 weight ratio and ground together into a fine powder using a mortar and pestle. Using a tube furnace, the powder was then annealed at 1000°C for 30 minutes at a 20°C/min ramp rate with argon flowing at 100 sccm.

3.2.5 Synthesis of SG Supported Pt-Ni Nanoparticles

Deposition of platinum nanoparticles onto SG was achieved via ethylene glycol and the polyol process, [74] and this catalyst is denoted as Pt/SG. The PtNi/SG alloy was synthesized by annealing the Pt/SG with nickel (II) nitrate hexahydrate in a 1:3 Pt-Ni molar ratio at 600°C for 7 h in a 100 sccm flow rate of 10%H_2-Ar and 10°C/min heating rate. The PtNi/SG was chemically dealloyed with 0.5 M sulphuric acid at 80°C for 24 hours, denoted as PtNi/SG-DA. Post heat treatment of the PtNi/SG-DA was performed at 400°C for 1 hour in similar conditions as above, denoted as PtNi/SG-PHT.

The overall synthesis procedure can be observed in *Figure* 3.1 below.

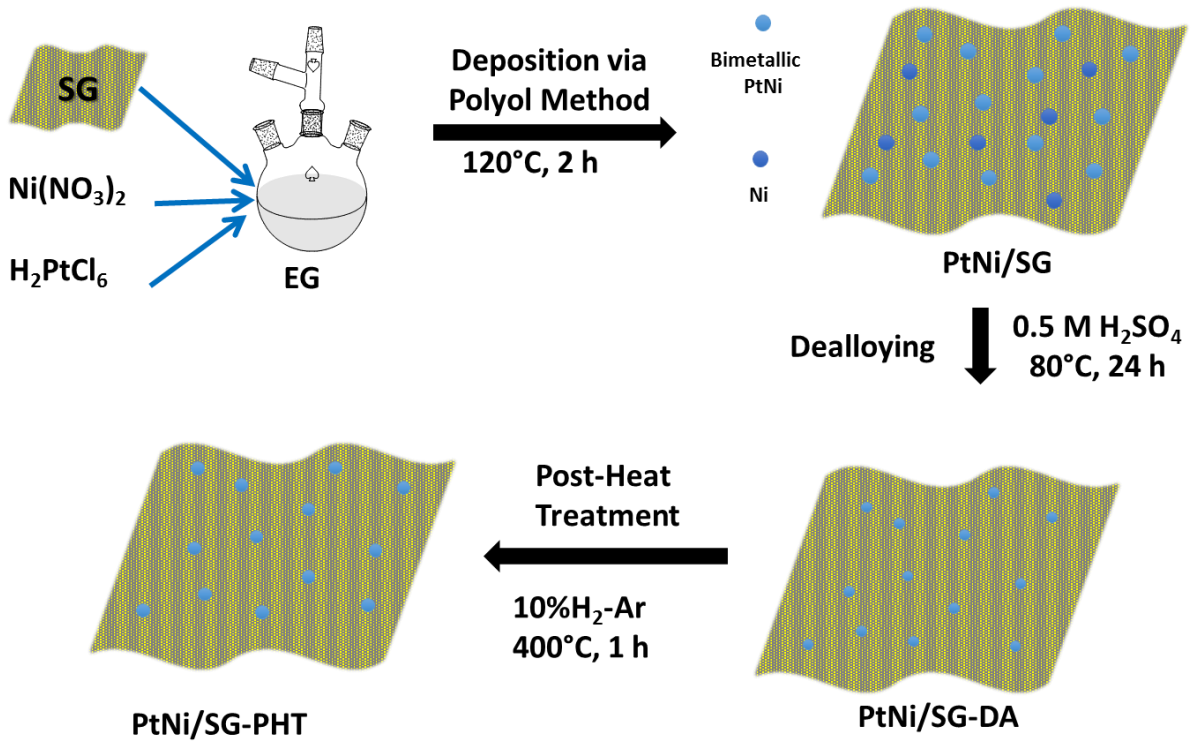

Figure 3.1: Overall synthesis scheme for the PtNi loaded sulfur-doped graphene electrocatalysts at various points in the procedure.

3.3 Results and Discussion

3.3.1 Physico-Chemical Characterization

TEM images of the samples Pt-Ni/SG, Pt-Ni/SG-DA and Pt-Ni/SG-PHT reveal the morphology of the electrocatalyst as subsequent preparation techniques are performed. These images can be seen progressively in Figure 1(a-c) with the associated particle size distributions shown in Figure 1(d-f). The morphology of SG itself is shown through SEM in Figure A1(a) (appendix), and the presence of sulfur in the sheets is confirmed in Figure A1(b) (appendix). It can be observed that the freshly prepared Pt-Ni/SG has a comparably broader particle size distribution than that of the others and this is due to the high temperature at which annealing was performed. Compared to the alloy particles with a wide distribution from 3-10 nm, the dealloyed

nanoparticles of Pt-Ni/SG-DA are noted to be diminished to a monodisperse diameter of approximately 2 nm. This size reduction is the result of transition metal leaching from the particles, leaving platinum as the dominant species. This concurs with literature findings where particles of this size were noted to be etched to smaller diameters after dealloying rather than form nanoporous particles of the same size. [30][126] Following a second heat treatment of the dealloyed sample for the Pt-Ni/SG-PHT catalyst, it can be seen from the size distribution that such a treatment has again stimulated a growth in particle size and a broadening of the distribution to 2-7 nm. However, the mean particle size as well as the spread in diameter is smaller than that of the alloyed particles as the post-heat treatment was not as great in temperature or exposure time as the first treatment step.

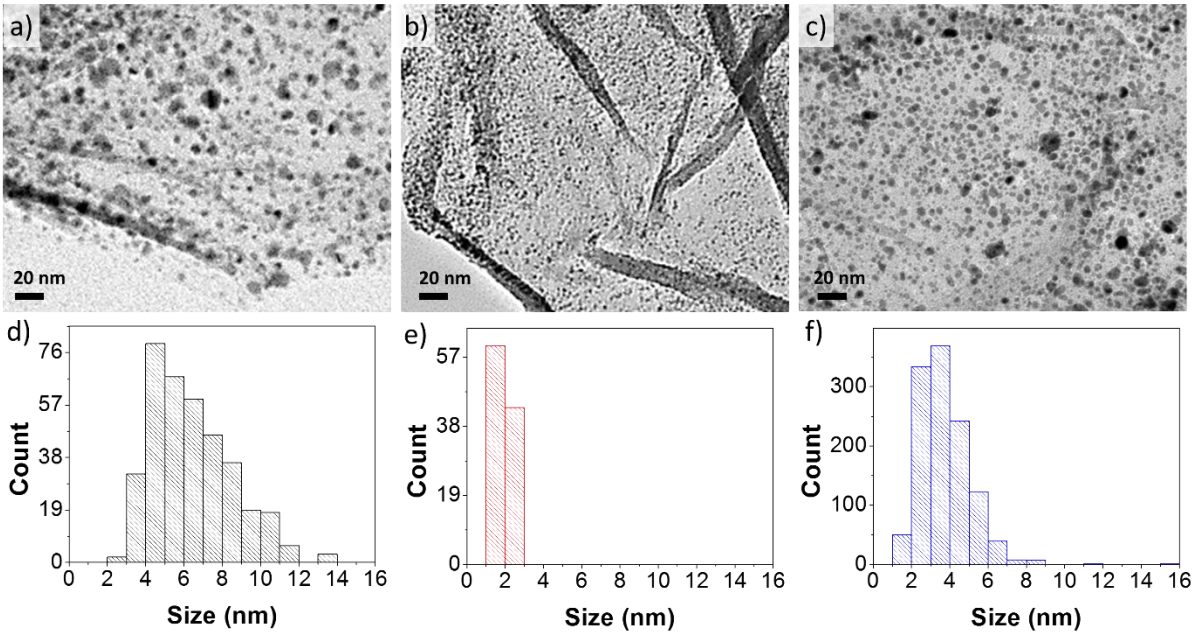

Figure 3.2. TEM imaging of the (a) Pt-Ni/SG, (b) Pt-Ni/SG-DA and (c) Pt-Ni/SG-PHT electrocatalysts. Particle size distributions of these catalysts are shown below the respective microscopy images, with (d) Pt-Ni/SG, (e) Pt-Ni/SG-DA and (f) Pt-Ni/SG-PHT.

The morphologies of the catalysts after ADT can be seen in Figure 2(a-c), and their corresponding size distributions are shown in Figure 2(d-f). From the particle size distributions of the three catalysts, it is clear that ADT has the effect of increasing the size of the metal particles. This observation concurs with well-known mechanisms of catalyst degradation such as migration of platinum and Ostwald ripening. [127] The size increase is most prevalent in Pt-Ni/SG, with the small <4 nm particles absent in Pt-Ni/SG-ADT. The maximum size of the Pt-Ni/SG-DA particles increases to 8 nm after ADT, and it is obvious that the size monodispersity of 2 nm is lost. It is interesting to note that the distributions of Pt-Ni/SG-PHT and Pt-Ni/SG-PHT-ADT differ very little, indicating the stability of this catalyst. Following the annealing step, the catalyst becomes very resistant to further changes in the size of the particles and the durability of Pt-Ni/SG-PHT is noted to be the greatest. On the other hand, the particle growth rate of Pt/C, shown in Figure A2 (appendix), is much more pronounced than that of Pt-Ni/SG-PHT. Through ICP analysis, the metal content was determined for each of the freshly synthesized catalysts. From Table S1 (appendix), it can be seen that a platinum loading of approximately 10wt% was achieved. After chemical dealloying, nickel leached from the particles and the absence of the metal after characterization is expected. There is also a minute loss in platinum from this technique. After post-heat treatment, extant functional groups such as –OH moieties are removed from the graphene support and hence, an increase in both nickel and platinum content can be seen. From the XRD spectra of the catalysts in Figure A3 (appendix), the peaks in Pt-Ni/SG indicates the presence of Ni particles during synthesis of the platinum-nickel alloy. However, after the leaching of nickel by dealloying for Pt-Ni/SG-DA and post-heat treatment for Pt-Ni/SG-PHT, well defined peaks related to Pt (111) can be observed. A qualitative visualization of the composition changes can be seen via elemental mapping in Figures A5 to A10 (appendix).

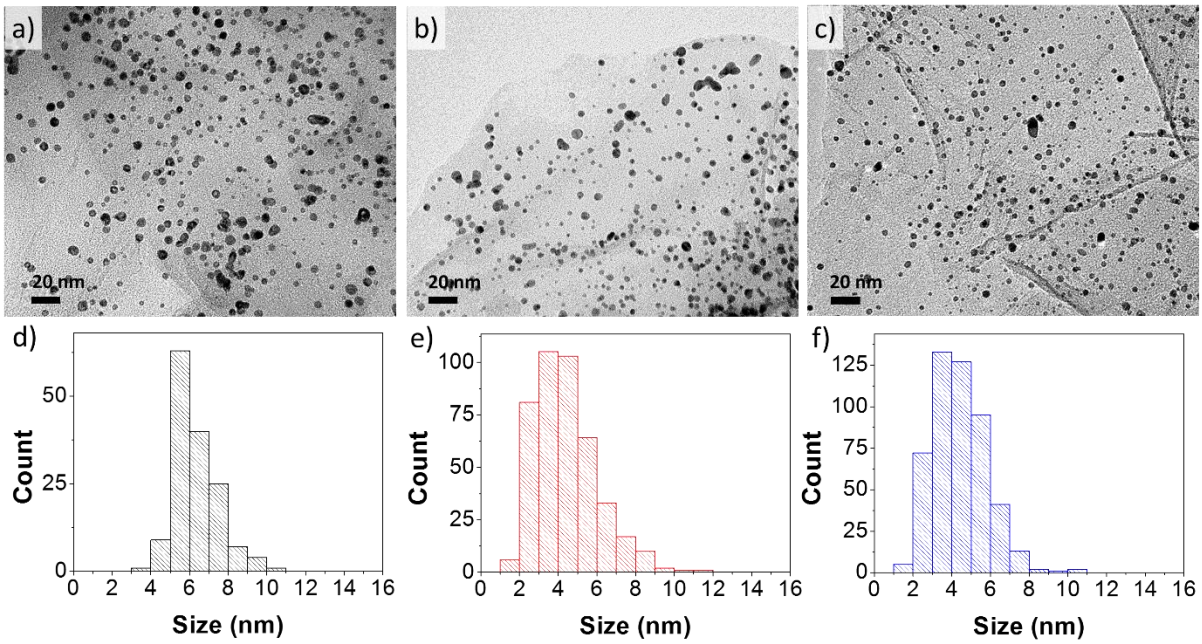

Figure 3.3. TEM imaging of the (a) Pt-Ni/SG-ADT, (b) Pt-Ni/SG-DA-ADT and (c) Pt-Ni/SG-PHT-ADT electrocatalysts. Particle size distributions of these catalysts are shown below the respective microscopy images, with (d) Pt-Ni/SG-ADT, (e) Pt-Ni/SG-DA-ADT and (f) Pt-Ni/SG-PHT-ADT.

3.3.2 Electrochemical Characterization

Pre- and post-ADT CVs from 0.05 to 1.3 V vs RHE for the as-prepared catalysts Pt-Ni/SG, Pt-Ni/SG-DA and Pt-Ni/SG-PHT as well as the commercial Pt/C are shown in Figure 3(a-d). The pre- and post-ADT ECSA as shown in Figure 3(e) were respectively 23.0 and 7.6 m^2/g for Pt-Ni/SG, 28.1 and 18.4 m^2/g for Pt-Ni/SG-DA, 23.0 and 16.7 m^2/g for Pt-Ni/SG-PHT and 45.3 m^2/g and 18.3 m^2/g for Pt/C. The normalized ECSA of the catalysts can be seen in Figure 3(f), and the percent loss in ECSA after ADT was 66, 34, 27 and 59% for Pt-Ni/SG-ADT, Pt-Ni/SG-DA-ADT, Pt-Ni/SG-PH-ADT and commercial Pt/C respectively. The increase in ECSA from the alloy to dealloyed catalyst can be correlated with the particle size distributions of the two, with the latter having particles at a relatively monodisperse 2-3 nm diameter. Finally, the thermal treatment of the dealloyed catalyst to form Pt-Ni/SG-PHT lead not only to particle size growth but also a

correlated decrease in ECSA similar to that of the alloy catalyst. The ECSA change following ADT clearly shows the greater stability of Pt-Ni/SG-PHT, and this retention can be attributed to the metal particle stabilization to SG following post-heat treatment. Thus, the benefits of SG lie in the strong interactions created between Pt and SG.

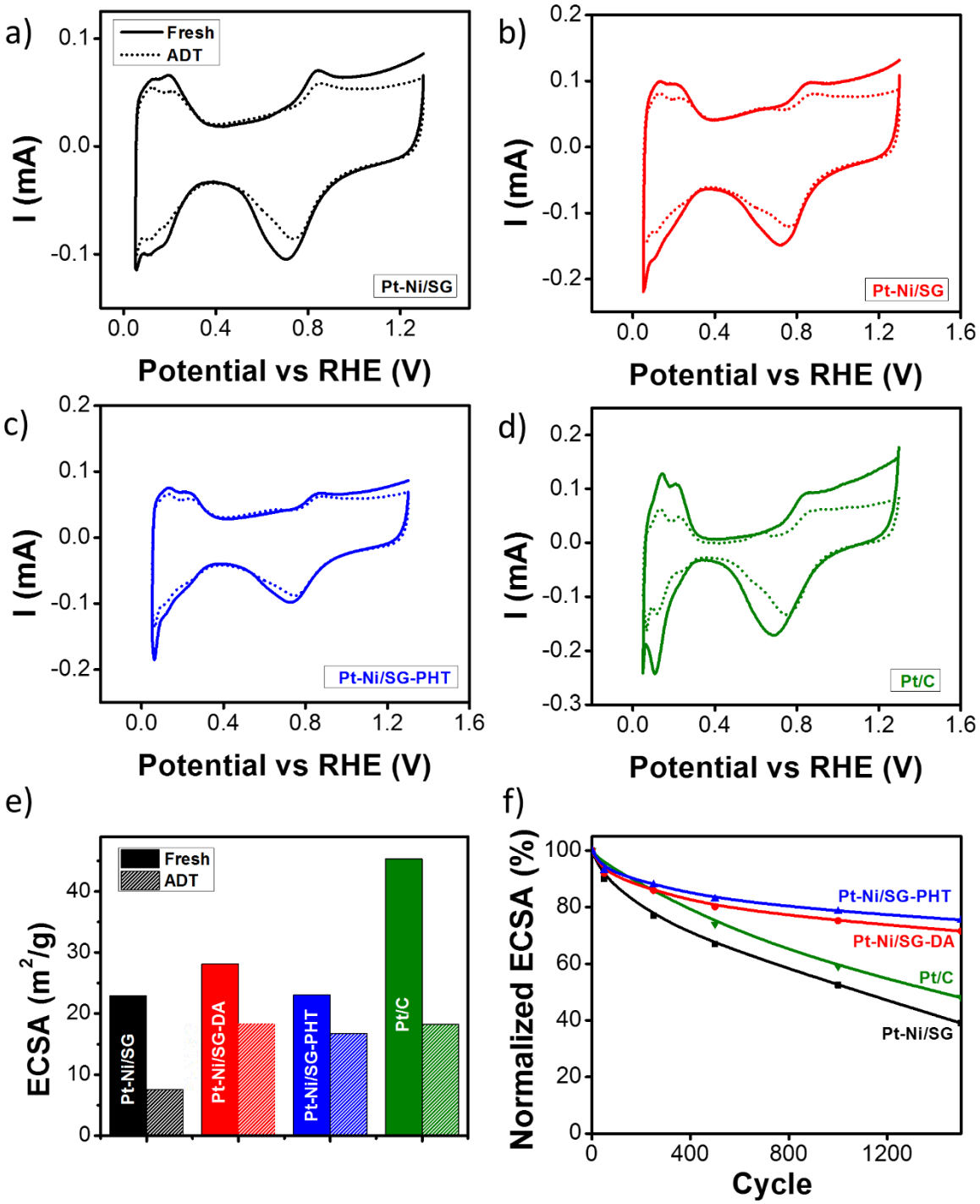

Figure 3.4. CV at 50 mV/s in N_2-saturated 0.1 M $HClO_4$, before and after ADT of 1500 cycles from 0.05 to 1.3 V, for a) alloyed Pt-Ni/SG, b) dealloyed Pt-Ni/SG-DA, c) post-heat treated Pt-Ni/SG-PHT and d) commercial Pt/C using a 0.196 cm^2 glassy carbon working electrode and Pt wire counter electrode. Catalyst stability comparison through e) absolute ECSA and f) normalized ECSA as a function of potential cycling.

The ORR polarization curves of the catalysts can be seen in Figure 4(a-d). From the limiting current in each catalyst, the mass-transport corrected kinetic current was derived to obtain the respective mass activities. The change in half-wave potentials for Pt-Ni/SG, Pt-Ni/SG-DA and Pt-Ni/SG-PHT were 38.7, 32.2 and 8.4 mV respectively, compared to 46.8 mV for Pt/C. The initial mass activity calculated at 0.9 V vs RHE of Pt-Ni/SG, Pt-Ni/SG-DA, Pt-Ni/SG-PHT, and Pt/C was 190, 153, 93 and 125 mA/mg_{Pt} respectively, while the mass activity after ADT was 42, 55, 67, and 39 mA/mg_{Pt} respectively, shown in Figure 4(e). This means that mass activity loss is respectively 77.9, 64.1, 28.0 and 68.8%. Similarly, the specific activities at 0.9 V vs RHE of Pt-Ni/SG, Pt-Ni/SG-DA, and Pt-Ni/SG-PHT were 829, 544, and 405 $\mu A/cm^2_{Pt}$ respectively which were higher than that of Pt/C at 266 $\mu A/cm^2_{Pt}$. The specific activities of these catalysts from 0.85 to 0.95 V vs RHE are displayed in Figure 4(f). The platinum content in the alloy catalyst as determined via ICP analysis was relatively low due to the dominance of nickel in the metal content, and this deficiency is expected to be a major factor in its limited activity improvement over Pt/C. The poor stability of Pt-Ni/SG with respect to mass activity is attributed to dissolution of the transition metal under the electrochemical conditions as indicated by Pourbaix diagrams, [128] which is to be compared to the greater resilience in more noble metals such as Pd. [7][129] After chemically-induced nickel leaching to form the Pt-Ni/SG-DA, there is a decrease in mass activity as compared to the alloy due to the loss of favourable phenomena provided by the transition metal including strain and ligand effects. Despite a lower initial mass activity than the alloy, the dealloyed catalyst suffered from a smaller activity loss as there was no significant nickel present for dissolution to occur from the nanoparticles. The increase in particle size for Pt-Ni/SG-PHT finally yields the lowest activity of the three electrocatalysts, but the thermal exposure also resulted in the highest interaction between the particles and catalyst support. As such, it has the highest

stability and its loss in activity is the smallest of all. Overall, the increased durability of Pt-Ni/SG-PHT over Pt/C can be attributed to the thiophenic sulfur moieties in the support material, which has previously been observed to be the source of strong binding between Pt and the doped graphene due to electronic structure modifications and strong catalyst-support interactions. [94]–[96] Such thiophene-like sulfur has also been previously identified experimentally through XPS spectra of SG used as a Pt-free catalyst, [130] though prior conclusions with regards to stability can only be inferred as the sulfur-carbon bonds preventing carbon corrosion upon which Pt nucleation sites reside. [131]

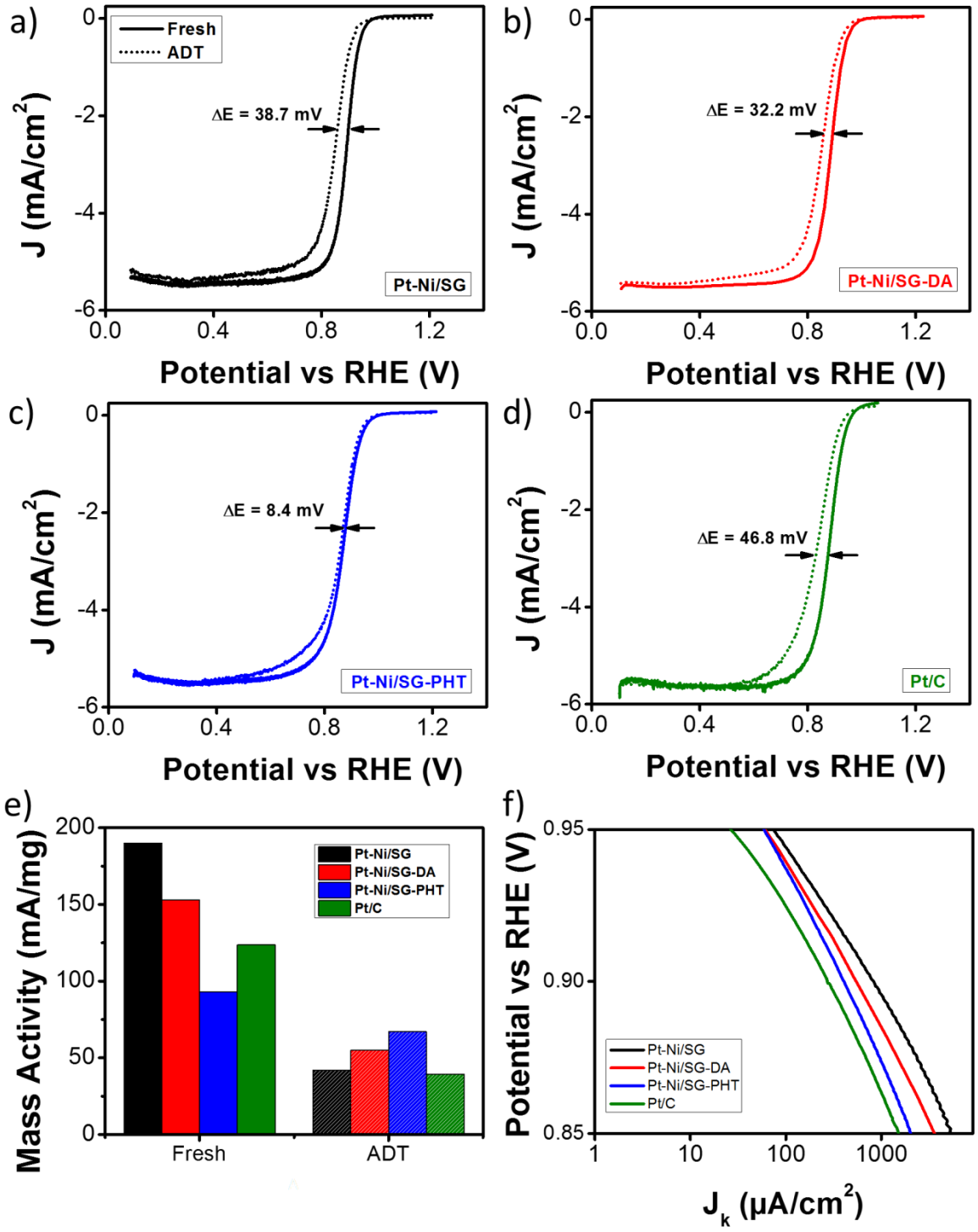

Figure 3.5. ORR polarization curves at 5 mV/s in O_2-saturated 0.1 M $HClO_4$, before and after ADT of 1500 cycles from 0.05 to 1.3 V, for a) alloyed Pt-Ni/SG, b) dealloyed Pt-Ni/SG-DA, c) post-heat treated Pt-Ni/SG-PHT and d) commercial TKK Pt/C (28.2wt% Pt) using a 0.196 cm^2 glassy carbon working electrode and Pt wire counter electrode. The prepared catalysts are compared to

commercial Pt/C through e) mass activity change before and after ADT, and f) specific activities from 0.85 to 0.95 V.

3.4 Summary

In summary, platinum-nickel alloy nanoparticles supported by SG were prepared and the physico-chemical as well as electrochemical characterization as per half-cell conditions was performed. This was done for the catalyst in its alloyed, dealloyed, and post-heat treated form with Pt-Ni/SG-PHT being found to have superior stability as it has the greatest retention in both ECSA and mass activity, with only a 27% loss in the former and a 28% loss in the latter. This is compared to a 59% ECSA loss and 69% activity loss for commercial Pt/C. The exceptional stability of Pt-Ni/SG-PHT demonstrates the Pt-SG interaction effects from sulfur doping to provide a highly durable catalyst support for the PEMFC cathode.

Chapter 4 — Conclusions and Future Work

In this work, the use of sulfur-doped graphene as a support material was observed to enhance the catalytic durability of bimetallic catalyst particles when compared to state of the art Pt/C in RDE conditions. The electrocatalyst incorporated Pt and Ni deposited on the SG support material as alloy nanoparticles by the polyol method, with acid leaching removing poorly active excess Ni and post heat treatment to anneal the leached metal particles. TEM imaging for each of these stages of synthesis before and after electrochemical testing revealed the physical changes in the deposited nanoparticles. In particular, a growth in particle size was noted for each stage after ADT but the dealloyed and post-heat treated particles experienced a much less pronounced change in size. This indicates a greater resistance to growth phenomena such as Ostwald ripening and sintering, which are the main concerns to the stability of commercial Pt/C. The presence and interactions between Pt and Ni were both confirmed using EDX, XPS, and ICP with the absence of Ni indicating successful leaching of the transition metal. From these techniques, it was also determined that the alloy particles had a high proportion of Ni relative to Pt, which could have impacted the final electrocatalytic activity due to the inherently poor catalysis of pure Ni. XRD spectra for the three stages of synthesis also corroborated with the acid leaching of Ni from the sample, with the peaks in the spectra shifting after Ni dissolution. Electrochemical testing in a half-cell setup revealed that the final stage of the catalyst Pt-Ni/SG-PHT exhibited greater stability than commercial Pt/C in ADT conditions of 1500 cycles from 0.05 to 1.3 V vs RHE. The Pt-Ni/SG-PHT catalyst experienced a 27% loss in ECSA from 23.0 m^2/g to 16.7 m^2/g, while Pt/C suffered a 59% loss from 45.3 m^2/g to 18.3 m^2/g. Similarly, the mass activity of the Pt-Ni/SG-PHT catalyst decreased by 28.0% from 93 mA/mg_{Pt} to 67 mA/mg_{Pt}, while that of Pt/C deteriorated by 68.8% from 125 mA/mg_{Pt} to 39 mA/mg_{Pt}.

From here, there are several directions from which more comprehensive findings can be made. In order to fully investigate the PtNi alloy particles deposited on SG support materials as in this work, more definitive electrochemical testing can be conducted. While RDE is a robust electrochemical characterization technique, practical results from fuel cell testing under MEA conditions would provide the most reliable information regarding the performance of the electrocatalyst. For this to happen, future work would also require large batch synthesis techniques to produce enough catalyst for MEA fabrication. This may require modifications to the synthesis procedure beyond the straightforward polyol method of metal deposition.

As indicated in *Chapter 1 — Introduction*, previous work involving SG suggests a synergistic phenomenon between the active metal material and the support material which leads to an increase in activity and durability. However, these findings have only involved pure Pt as the metal component. Because of the many mechanisms involved in the catalytic enhancement of multimetallic alloys, it would be of great interest to study the use of doped graphene-based materials when other transition metals such as Cu, Co or Fe are involved. Furthermore, facet-controlled synthesis could garner additional attention, as literature has shown that the most active facet for pure Pt is not necessarily the most active in a binary alloy catalyst as with Pt(110) as compared to PtNi(111). With all of these factors in mind, the optimal catalyst incorporating multimetallic alloy particles deposited onto a sulfur-doped graphene support can be comprehensively understood in future work.

References

[1] J. K. Nørskov, J. Rossmeisl, A. Logadottir, L. Lindqvist, J. R. Kitchin, T. Bligaard, and H. Jónsson, "Origin of the overpotential for oxygen reduction at a fuel-cell cathode," *J. Phys. Chem. B*, vol. 108, no. 46, pp. 17886–17892, 2004.

[2] T. Bligaard and J. K. Nørskov, "Ligand effects in heterogeneous catalysis and electrochemistry," *Electrochim. Acta*, vol. 52, no. 18, pp. 5512–5516, May 2007.

[3] E. Toyoda, R. Jinnouchi, T. Hatanaka, Y. Morimoto, K. Mitsuhara, A. Visikovskiy, and Y. Kido, "The d-band structure of Pt nanoclusters correlated with the catalytic activity for an oxygen reduction reaction," *J. Phys. Chem. C*, vol. 115, no. 43, pp. 21236–21240, 2011.

[4] I. E. L. Stephens, A. S. Bondarenko, U. Grønbjerg, J. Rossmeisl, and I. Chorkendorff, "Understanding the electrocatalysis of oxygen reduction on platinum and its alloys," *Energy Environ. Sci.*, vol. 5, no. 5, p. 6744, 2012.

[5] V. Stamenkovic, B. S. Mun, K. J. J. Mayrhofer, P. N. Ross, N. M. Markovic, J. Rossmeisl, J. Greeley, and J. K. Nørskov, "Changing the activity of electrocatalysts for oxygen reduction by tuning the surface electronic structure," *Angew. Chemie Int. Ed.*, vol. 45, no. 18, pp. 2897–2901, 2006.

[6] J. R. Kitchin, J. K. Nørskov, M. A. Barteau, and J. G. Chen, "Modification of the surface electronic and chemical properties of Pt(111) by subsurface 3d transition metals," *J. Chem. Phys.*, vol. 120, no. 21, pp. 10240–10246, Jun. 2004.

[7] L. Zhang, S. Zhu, Q. Chang, D. Su, J. Yue, Z. Du, and M. Shao, "Palladium–Platinum Core–Shell Electrocatalysts for Oxygen Reduction Reaction Prepared with the Assistance of Citric Acid," *ACS Catal.*, pp. 3428–3432, 2016.

[8] J. Solla-Gull?n, A. Rodes, V. Montiel, A. Aldaz, and J. Clavilier, "Electrochemical characterisation of platinum?palladium nanoparticles prepared in a water-in-oil microemulsion," *J. Electroanal. Chem.*, vol. 554–555, no. 1, pp. 273–284, Sep. 2003.

[9] H. Ye and R. M. Crooks, "Effect of elemental composition of PtPd bimetallic nanoparticles containing an average of 180 atoms on the kinetics of the electrochemical oxygen reduction reaction," *J. Am. Chem. Soc.*, vol. 129, no. 12, pp. 3627–3633, 2007.

[10] S. M. Alia, K. O. Jensen, B. S. Pivovar, and Y. Yan, "Platinum-coated palladium nanotubes as oxygen reduction reaction electrocatalysts," *ACS Catal.*, vol. 2, no. 5, pp. 858–863, 2012.

[11] G. Zhang, Z. G. Shao, W. Lu, G. Li, F. Liu, and B. Yi, "One-pot synthesis of Ir@Pt nanodendrites as highly active bifunctional electrocatalysts for oxygen reduction and oxygen evolution in acidic medium," *Electrochem. commun.*, vol. 22, no. 1, pp. 145–148, 2012.

[12] K. M. Yeo, S. Choi, R. M. Anisur, J. Kim, and I. S. Lee, "Surfactant-free platinum-on-gold nanodendrites with enhanced catalytic performance for oxygen reduction," *Angew. Chemie - Int. Ed.*, vol. 50, no. 3, pp. 745–748, 2011.

[13] Y. Dai, L. Ou, W. Liang, F. Yang, Y. Liu, and S. Chen, "Efficient and superiorly durable Pt-lean electrocatalysts of Pt-W alloys for the oxygen reduction reaction," *J. Phys. Chem. C*, vol. 115, no. 5, pp. 2162–2168, 2011.

[14] Y. Liang, S. Lin, C. Liu, S. Chung, T. Chen, J.-H. Wang, and K. Wang, "The performance and stability of the oxygen reduction reaction on Pt–M (M = Pd, Ag and Au) nanorods: an experimental and computational study," *Chem. Commun.*, vol. 51, no. 30, pp. 6605–6608, 2015.

[15] E. Antolini, R. R. Passos, and E. A. Ticianelli, "Electrocatalysis of oxygen reduction on a carbon supported platinum-vanadium alloy in polymer electrolyte fuel cells," *Electrochim. Acta*, vol. 48, no. 3, pp. 263–270, 2002.

[16] L. Xiong, K. L. More, and T. He, "Syntheses, characterization, and catalytic oxygen electroreduction activities of carbon-supported PtW nanoparticle catalysts," *J. Power Sources*, vol. 195, no. 9, pp. 2570–2578, 2010.

[17] J. Greeley, I. E. L. Stephens, a S. Bondarenko, T. P. Johansson, H. a Hansen, T. F. Jaramillo, J. Rossmeisl, I. Chorkendorff, and J. K. Nørskov, "Alloys of platinum and early transition metals as

oxygen reduction electrocatalysts.," *Nat. Chem.*, vol. 1, no. 7, pp. 552–556, 2009.
[18] P. Hernandez-Fernandez, F. Masini, D. N. McCarthy, C. E. Strebel, D. Friebel, D. Deiana, P. Malacrida, A. Nierhoff, A. Bodin, A. M. Wise, J. H. Nielsen, T. W. Hansen, A. Nilsson, I. E. L. Stephens, and I. Chorkendorff, "Mass-selected nanoparticles of PtxY as model catalysts for oxygen electroreduction," *Nat. Chem.*, vol. 6, no. 8, pp. 732–738, 2014.
[19] X. Huang, Z. Zhao, L. Cao, Y. Chen, E. Zhu, Z. Lin, M. Li, A. Yan, A. Zettl, Y. M. Wang, X. Duan, T. Mueller, and Y. Huang, "High-performance transition metal-doped Pt3Ni octahedra for oxygen reduction reaction," *Science (80-.).*, vol. 348, no. 6240, pp. 1230–1234, Jun. 2015.
[20] J. Liu, C. Xu, C. Liu, F. Wang, H. Liu, J. Ji, and Z. Li, "Impact of Cu-Pt nanotubes with a high degree of alloying on electro-catalytic activity toward oxygen reduction reaction," *Electrochim. Acta*, vol. 152, pp. 425–432, 2015.
[21] I. Spanos, J. J. K. Kirkensgaard, K. Mortensen, and M. Arenz, "Investigating the activity enhancement on PtxCo1−x alloys induced by a combined strain and ligand effect," *J. Power Sources*, vol. 245, pp. 908–914, Jan. 2014.
[22] M. Shao, J. H. Odell, A. Peles, and D. Su, "The role of transition metals in the catalytic activity of Pt alloys: quantification of strain and ligand effects.," *Chem. Commun. (Camb).*, vol. 50, no. 17, pp. 2173–6, 2014.
[23] S. Il Choi, S. Xie, M. Shao, N. Lu, S. Guerrero, J. H. Odell, J. Park, J. Wang, M. J. Kim, and Y. Xia, "Controlling the size and composition of nanosized Pt-Ni octahedra to optimize their catalytic activities toward the oxygen reduction reaction," *ChemSusChem*, vol. 7, no. 5, pp. 1476–1483, 2014.
[24] F. Maroun, "The Role of Atomic Ensembles in the Reactivity of Bimetallic Electrocatalysts," *Science (80-.).*, vol. 293, no. 5536, pp. 1811–1814, Sep. 2001.
[25] E. Antolini, T. Lopes, and E. R. Gonzalez, "An overview of platinum-based catalysts as methanol-resistant oxygen reduction materials for direct methanol fuel cells," *J. Alloys Compd.*, vol. 461, no. 1–2, pp. 253–262, 2008.
[26] M. Chen, "The Promotional Effect of Gold in Catalysis by Palladium-Gold," *Science (80-.).*, vol. 310, no. 5746, pp. 291–293, 2005.
[27] P. Liu and J. K. Nørskov, "Ligand and ensemble effects in adsorption on alloy surfaces," *Phys. Chem. Chem. Phys.*, vol. 3, no. 17, pp. 3814–3818, 2001.
[28] B. Du and Y. Tong, "A coverage-dependent study of Pt spontaneously deposited onto Au and Ru surfaces: Direct experimental evidence of the ensemble effect for methanol electro-oxidation on Pt," *J. Phys. Chem. B*, vol. 109, no. 38, pp. 17775–17780, 2005.
[29] Y. Deng, V. Tripkovic, J. Rossmeisl, and M. Arenz, "Oxygen Reduction Reaction on Pt Overlayers Deposited onto a Gold Film : Ligand , Strain , and Ensemble E ff ect," 2016.
[30] L. Gan, M. Heggen, R. O. Malley, B. Theobald, P. Strasser, R. O'Malley, B. Theobald, and P. Strasser, "Understanding and controlling nanoporosity formation for improving the stability of bimetallic fuel cell catalysts," *Nano Lett.*, vol. 13, no. 3, pp. 1131–1138, 2013.
[31] A. Wieckowski, *FUEL CELL SCIENCE Wiley Series on Electrocatalysis and Electrochemistry*. Hoboken: Wiley, 2010.
[32] V. Mazumder, Y. Lee, and S. Sun, "Recent development of active nanoparticle catalysts for fuel cell reactions," *Adv. Funct. Mater.*, vol. 20, no. 8, pp. 1224–1231, 2010.
[33] Z. Liu, L. Ma, J. Zhang, K. Hongsirikarn, and J. G. Goodwin, "Pt Alloy Electrocatalysts for Proton Exchange Membrane Fuel Cells: A Review," *Catal. Rev.*, vol. 55, no. 3, pp. 255–288, 2013.
[34] M. Shao, *Electrocatalysis in Fuel Cells*, vol. 9. London: Springer London, 2013.
[35] M. Watanabe and S. Motoo, "Electrocatalysis by ad-atoms," *J. Electroanal. Chem. Interfacial Electrochem.*, vol. 60, no. 3, pp. 267–273, Apr. 1975.
[36] H. Yang, J. Zhang, S. Kumar, H. Zhang, R. Yang, J. Fang, and S. Zou, "Monodisperse and highly active PtNi nanoparticles for O2 reduction," *Electrochem. commun.*, vol. 11, no. 12, pp. 2278–2281, 2009.
[37] Y. Huang, J. Zhang, A. Kongkanand, F. T. Wagner, J. C. M. Li, and J. Jorne, "Transient Platinum

Oxide Formation and Oxygen Reduction on Carbon-Supported Platinum and Platinum-Cobalt Alloy Electrocatalysts," *J. Electrochem. Soc.*, vol. 161, no. 1, pp. F10–F15, 2013.
[38] S. Senthil Kumar and K. L. N. Phani, "Exploration of unalloyed bimetallic Au-Pt/C nanoparticles for oxygen reduction reaction," *J. Power Sources*, vol. 187, no. 1, pp. 19–24, 2009.
[39] K. Miecznikowski, P. J. Kulesza, and S. Fiechter, "Application of Black Pearl carbon-supported WO3 nanostructures as hybrid carriers for electrocatalytic RuSex nanoparticles," *Appl. Surf. Sci.*, vol. 257, no. 19, pp. 8215–8222, 2011.
[40] B. Dembinska, M. Kiliszek, H. Elzanowska, M. Pisarek, and P. J. Kulesza, "Enhancement of activity of RuSex electrocatalyst by modification with nanostructured iridium towards more efficient reduction of oxygen," *J. Power Sources*, vol. 243, pp. 225–232, 2013.
[41] J. B. Xu, T. S. Zhao, W. W. Yang, and S. Y. Shen, "Effect of surface composition of Pt-Au alloy cathode catalyst on the performance of direct methanol fuel cells," *Int. J. Hydrogen Energy*, vol. 35, no. 16, pp. 8699–8706, 2010.
[42] L. Guo, L.-B. Huang, W.-J. Jiang, Z.-D. Wei, L.-J. Wan, and J.-S. Hu, "Tuning the branches and composition of PtCu nanodendrites through underpotential deposition of Cu towards advanced electrocatalytic activity," *J. Mater. Chem. A*, vol. 5, no. 19, pp. 9014–9021, 2017.
[43] C. Wang, M. Chi, D. Li, D. van der Vliet, G. Wang, Q. Lin, J. F. Mitchell, K. L. More, N. M. Markovic, V. R. Stamenkovic, J. F. Mitchell, K. L. More, N. M. Markovic, and V. R. Stamenkovic, "Synthesis of Homogeneous Pt-Bimetallic Nanoparticles as Highly Efficient Electrocatalysts," *ACS Catal.*, vol. 1, no. 10, pp. 1355–1359, Oct. 2011.
[44] V. R. Stamenkovic, B. S. Mun, M. Arenz, K. J. J. Mayrhofer, C. A. Lucas, G. Wang, P. N. Ross, and N. M. Markovic, "Trends in electrocatalysis on extended and nanoscale Pt-bimetallic alloy surfaces," *Nat. Mater.*, vol. 6, no. 3, pp. 241–247, 2007.
[45] W. Chen, J. M. Kim, S. H. Sun, and S. W. Chen, "Electrocatalytic reduction of oxygen by FePt alloy nanoparticles," *J. Phys. Chem. C*, vol. 112, no. 10, pp. 3891–3898, 2008.
[46] C. Wang, M. Chi, G. Wang, D. Van Der Vliet, D. Li, K. More, H. H. Wang, J. A. Schlueter, N. M. Markovic, and V. R. Stamenkovic, "Correlation between surface chemistry and electrocatalytic properties of monodisperse PtxNi1-x nanoparticles," *Adv. Funct. Mater.*, vol. 21, no. 1, pp. 147–152, 2011.
[47] R. O'Hayre, S.-W. Cha, W. Colella, and F. B. Prinz, *Fuel Cell Fundamentals*. Hoboken, NJ, USA: John Wiley & Sons, Inc, 2016.
[48] I. N. Leontyev, S. V. Belenov, V. E. Guterman, P. Haghi-Ashtiani, A. P. Shaganov, and B. Dkhil, "Catalytic activity of Carbon-supported pt nanoelectrocatalysts. Why reducing the size of pt nanoparticles is not always beneficial," *J. Phys. Chem. C*, vol. 115, no. 13, pp. 5429–5434, 2011.
[49] F. J. Perez-Alonso, D. N. McCarthy, A. Nierhoff, P. Hernandez-Fernandez, C. Strebel, I. E. L. Stephens, J. H. Nielsen, and I. Chorkendorff, "The effect of size on the oxygen electroreduction activity of mass-selected platinum nanoparticles," *Angew. Chemie - Int. Ed.*, vol. 51, no. 19, pp. 4641–4643, 2012.
[50] E. Antolini, "Structural parameters of supported fuel cell catalysts: The effect of particle size, inter-particle distance and metal loading on catalytic activity and fuel cell performance," *Appl. Catal. B Environ.*, vol. 181, pp. 298–313, 2016.
[51] H. A. Gasteiger, S. S. Kocha, B. Sompalli, and F. T. Wagner, "Activity benchmarks and requirements for Pt, Pt-alloy, and non-Pt oxygen reduction catalysts for PEMFCs," *Appl. Catal. B Environ.*, vol. 56, no. 1–2 SPEC. ISS., pp. 9–35, 2005.
[52] Z. Xu, H. Zhang, H. Zhong, Q. Lu, Y. Wang, and D. Su, "Effect of particle size on the activity and durability of the Pt/C electrocatalyst for proton exchange membrane fuel cells," *Appl. Catal. B Environ.*, vol. 111–112, pp. 264–270, 2012.
[53] H. Yano, J. Inukai, H. Uchida, M. Watanabe, P. K. Babu, T. Kobayashi, J. H. Chung, E. Oldfield, and A. Wieckowski, "Particle-size effect of nanoscale platinum catalysts in oxygen reduction reaction: an electrochemical and 195Pt EC-NMR study," *Phys. Chem. Chem. Phys.*, vol. 8, no. 42, p. 4932, 2006.

[54] K. Yamamoto, T. Imaoka, W.-J. Chun, O. Enoki, H. Katoh, M. Takenaga, and A. Sonoi, "Size-specific catalytic activity of platinum clusters enhances oxygen reduction reactions," *Nat. Chem.*, vol. 1, no. 5, pp. 397–402, 2009.
[55] F. Calle-Vallejo, J. I. Martínez, J. M. García-Lastra, P. Sautet, and D. Loffreda, "Fast prediction of adsorption properties for platinum nanocatalysts with generalized coordination numbers," *Angew. Chemie - Int. Ed.*, vol. 53, no. 32, pp. 8316–8319, 2014.
[56] O. Antoine and R. Durand, "RRDE study of oxygen reduction on Pt nanoparticles inside Nafion: H2O2 production in PEMFC cathode conditions," *J. Appl. Electrochem.*, vol. 30, no. 7, pp. 839–844, 2000.
[57] Y. Nie, L. Li, and Z. Wei, "Recent advancements in Pt and Pt-free catalysts," *Chem Soc Rev*, vol. 44, no. 8, pp. 2168–2201, 2015.
[58] C. Wang, H. Daimon, T. Onodera, T. Koda, and S. Sun, "A general approach to the size- and shape-controlled synthesis of platinum nanoparticles and their catalytic reduction of oxygen," *Angew. Chemie - Int. Ed.*, vol. 47, no. 19, pp. 3588–3591, 2008.
[59] V. Komanicky, H. Lddir, K. C. Chang, A. Menzel, G. Karapetrov, D. Hennessy, P. Zapol, and H. You, "Shape-dependent activity of platinum array catalyst," *J. Am. Chem. Soc.*, vol. 131, no. 16, pp. 5732–5733, 2009.
[60] V. R. Stamenkovic, B. Fowler, B. S. Mun, G. Wang, P. N. Ross, C. a Lucas, and N. M. Marković, "Improved oxygen reduction activity on Pt3Ni(111) via increased surface site availability.," *Science*, vol. 315, no. 5811, pp. 493–7, 2007.
[61] J. Wu, J. Zhang, Z. Peng, S. Yang, F. T. Wagner, and H. Yang, "Truncated Octahedral Pt 3 Ni Oxygen Reduction Reaction Electrocatalysts," *J. Am. Chem. Soc.*, vol. 132, no. 14, pp. 4984–4985, Apr. 2010.
[62] J. Zhang, H. Yang, J. Fang, and S. Zou, "Synthesis and oxygen reduction activity of shape-controlled Pt(3)Ni nanopolyhedra.," *Nano Lett.*, vol. 10, no. 2, pp. 638–644, 2010.
[63] M. K. Carpenter, T. E. Moylan, R. S. Kukreja, M. H. Atwan, and M. M. Tessema, "Solvothermal Synthesis of Platinum Alloy Nanoparticles for Oxygen Reduction Electrocatalysis," *J. Am. Chem. Soc.*, vol. 134, no. 20, pp. 8535–8542, May 2012.
[64] C. Chen, Y. Kang, Z. Huo, Z. Zhu, W. Huang, H. L. Xin, J. D. Snyder, D. Li, J. A. Herron, M. Mavrikakis, M. Chi, K. L. More, Y. Li, N. M. Markovic, G. A. Somorjai, P. Yang, and V. R. Stamenkovic, "Highly Crystalline Multimetallic Nanoframes with Three-Dimensional Electrocatalytic Surfaces," *Science (80-.).*, vol. 343, no. 6177, pp. 1339–1343, 2014.
[65] S. Il Choi, S. Xie, M. Shao, J. H. Odell, N. Lu, H. C. Peng, L. Protsailo, S. Guerrero, J. Park, X. Xia, J. Wang, M. J. Kim, and Y. Xia, "Synthesis and characterization of 9 nm Pt-Ni octahedra with a record high activity of 3.3 A/mgPt for the oxygen reduction reaction," *Nano Lett.*, vol. 13, no. 7, pp. 3420–3425, 2013.
[66] B. Lim, M. Jiang, P. H. C. Camargo, E. C. Cho, J. Tao, X. Lu, Y. Zhu, and Y. Xia, "Pd-Pt Bimetallic Nanodendrites with High Activity for Oxygen Reduction," *Science (80-.).*, vol. 324, no. 5932, pp. 1302–1305, Jun. 2009.
[67] D. Wang, H. L. Xin, R. Hovden, H. Wang, Y. Yu, D. A. Muller, F. J. DiSalvo, and H. D. Abruña, "Structurally ordered intermetallic platinum–cobalt core–shell nanoparticles with enhanced activity and stability as oxygen reduction electrocatalysts," *Nat. Mater.*, vol. 12, no. 1, pp. 81–87, 2012.
[68] M. Oezaslan, F. Hasché, and P. Strasser, "Pt-based core-shell catalyst architectures for oxygen fuel cell electrodes," *J. Phys. Chem. Lett.*, vol. 4, no. 19, pp. 3273–3291, 2013.
[69] M. Oezaslan, F. Hasché, and P. Strasser, "Pt-based core-shell catalyst architectures for oxygen fuel cell electrodes," *J. Phys. Chem. Lett.*, vol. 4, no. 19, pp. 3273–3291, 2013.
[70] V. R. Stamenkovic, B. S. Mun, K. J. J. Mayrhofer, P. N. Ross, and N. M. Markovic, "Effect of surface composition on electronic structure, stability, and electrocatalytic properties of Pt-transition metal alloys: Pt-skin versus Pt-skeleton surfaces," *J. Am. Chem. Soc.*, vol. 128, no. 27, pp. 8813–8819, 2006.

[71] Y. Wang and N. Toshima, “Preparation of Pd−Pt Bimetallic Colloids with Controllable Core/Shell Structures,” *J. Phys. Chem. B*, vol. 101, no. 27, pp. 5301–5306, 1997.
[72] D.-H. Lim, W.-J. Lee, J. Wheldon, N. L. Macy, and W. H. Smyrl, “Electrochemical Characterization and Durability of Sputtered Pt Catalysts on TiO[sub 2] Nanotube Arrays as a Cathode Material for PEFCs,” *J. Electrochem. Soc.*, vol. 157, no. 6, p. B862, 2010.
[73] Y.-J. Wang, D. P. Wilkinson, and J. Zhang, “Noncarbon Support Materials for Polymer Electrolyte Membrane Fuel Cell Electrocatalysts,” *Chem. Rev.*, vol. 111, no. 12, pp. 7625–7651, 2011.
[74] S. Sharma and B. G. Pollet, “Support materials for PEMFC and DMFC electrocatalysts - A review,” *J. Power Sources*, vol. 208, pp. 96–119, 2012.
[75] A. Masao, S. Noda, F. Takasaki, K. Ito, and K. Sasaki, “Carbon-Free Pt Electrocatalysts Supported on SnO[sub 2] for Polymer Electrolyte Fuel Cells,” *Electrochem. Solid-State Lett.*, vol. 12, no. 9, p. B119, 2009.
[76] B. Seger, A. Kongkanand, K. Vinodgopal, and P. V. Kamat, “Platinum dispersed on silica nanoparticle as electrocatalyst for PEM fuel cell,” *J. Electroanal. Chem.*, vol. 621, no. 2, pp. 198–204, 2008.
[77] H. Chhina, S. Campbell, and O. Kesler, “Ex situ Evaluation of Tungsten Oxide as a Catalyst Support for PEMFCs,” *J. Electrochem. Soc.*, vol. 154, no. 6, p. B533, 2007.
[78] R. B. Levy and M. Boudart, “Platinum-Like Behavior of Tungsten Carbide in Surface Catalysis,” *Science (80-.).*, vol. 181, no. 4099, pp. 547–549, 1973.
[79] Z. Yan, M. Cai, and P. K. Shen, “Nanosized tungsten carbide synthesized by a novel route at low temperature for high performance electrocatalysis,” *Sci. Rep.*, vol. 3, pp. 1–7, 2013.
[80] S. Zhang, H. Zhu, H. Yu, J. Hou, B. Yi, and P. Ming, “The oxidation resistance of tungsten carbide as catalyst support for proton exchange membrane fuel cells,” *Chinese J. Catal.*, vol. 28, no. 2, pp. 109–111, 2007.
[81] E. Antolini, “Carbon supports for low-temperature fuel cell catalysts,” *Appl. Catal. B Environ.*, vol. 88, no. 1–2, pp. 1–24, 2009.
[82] S. Park, Y. Shao, R. Kou, V. V. Viswanathan, S. A. Towne, P. C. Rieke, J. Liu, Y. Lin, and Y. Wang, “Polarization Losses under Accelerated Stress Test Using Multiwalled Carbon Nanotube Supported Pt Catalyst in PEM Fuel Cells,” *J. Electrochem. Soc.*, vol. 158, no. 3, p. B297, 2011.
[83] D. Higgins, P. Zamani, A. Yu, and Z. Chen, “The application of graphene and its composites in oxygen reduction electrocatalysis: a perspective and review of recent progress,” *Energy Environ. Sci.*, vol. 9, no. 2, pp. 357–390, 2016.
[84] K.-W. Park and K.-S. Seol, “Nb-TiO2 supported Pt cathode catalyst for polymer electrolyte membrane fuel cells,” *Electrochem. commun.*, vol. 9, no. 9, pp. 2256–2260, 2007.
[85] O. E. Haas, S. T. Briskeby, O. E. Kongstein, M. Tsypkin, R. Tunold, and B. T. Borresen, “Synthesis and Characterisation of Ru~ xTi~ x~-~ 1O~ 2 as a Catalyst Support for Polymer Electrolyte Fuel Cell,” *J. New Mater. Electrochem. Syst.*, vol. 11, no. 1, p. 9, 2008.
[86] K. S. Lee, I. S. Park, Y. H. Cho, D. S. Jung, N. Jung, H. Y. Park, and Y. E. Sung, “Electrocatalytic activity and stability of Pt supported on Sb-doped SnO2 nanoparticles for direct alcohol fuel cells,” *J. Catal.*, vol. 258, no. 1, pp. 143–152, 2008.
[87] H. Chhina, D. Susac, S. Campbell, and O. Kesler, “Transmission Electron Microscope Observation of Pt Deposited on Nb-Doped Titania,” *Electrochem. Solid-State Lett.*, vol. 12, no. 6, p. B97, 2009.
[88] S.-Y. Huang, P. Ganesan, and B. N. Popov, “Electrocatalytic activity and stability of niobium-doped titanium oxide supported platinum catalyst for polymer electrolyte membrane fuel cells,” *Appl. Catal. B Environ.*, vol. 96, no. 1–2, pp. 224–231, 2010.
[89] Y. Zheng, Y. Jiao, L. Ge, M. Jaroniec, and S. Z. Qiao, “Two-step boron and nitrogen doping in graphene for enhanced synergistic catalysis,” *Angew. Chemie - Int. Ed.*, vol. 52, no. 11, pp. 3110–3116, 2013.
[90] X. Sun, Y. Zhang, P. Song, J. Pan, L. Zhuang, W. Xu, and W. Xing, “Fluorine-Doped Carbon

Blacks: Highly Efficient Metal-Free Electrocatalysts for Oxygen Reduction Reaction," *ACS Catal.*, vol. 3, no. 8, pp. 1726–1729, Aug. 2013.
[91] J. Wu, Z. Yang, Q. Sun, X. Li, P. Strasser, and R. Yang, "Synthesis and electrocatalytic activity of phosphorus-doped carbon xerogel for oxygen reduction," *Electrochim. Acta*, vol. 127, pp. 53–60, 2014.
[92] Y. Zhou, K. Neyerlin, T. S. Olson, S. Pylypenko, J. Bult, H. N. Dinh, T. Gennett, Z. Shao, and R. O'Hayre, "Enhancement of Pt and Pt-alloy fuel cell catalyst activity and durability via nitrogen-modified carbon supports," *Energy Environ. Sci.*, vol. 3, no. 10, p. 1437, 2010.
[93] J.-Y. Choi, D. U. Lee, and Z. Chen, "Nitrogen-Doped Activated Graphene Supported Platinum Electrocatalyst for Oxygen Reduction Reaction in PEM Fuel Cells," *ECS Trans.*, vol. 50, no. 2, pp. 1815–1822, Mar. 2013.
[94] D. Higgins, M. A. Hoque, M. H. Seo, R. Wang, F. Hassan, J.-Y. Choi, M. Pritzker, A. Yu, J. Zhang, and Z. Chen, "Development and Simulation of Sulfur-doped Graphene Supported Platinum with Exemplary Stability and Activity Towards Oxygen Reduction," *Adv. Funct. Mater.*, vol. 24, no. 27, pp. 4325–4336, 2014.
[95] M. A. Hoque, F. M. Hassan, D. Higgins, J. Y. Choi, M. Pritzker, S. Knights, S. Ye, and Z. Chen, "Multigrain platinum nanowires consisting of oriented nanoparticles anchored on sulfur-doped graphene as a highly active and durable oxygen reduction electrocatalyst," *Adv. Mater.*, vol. 27, no. 7, pp. 1229–1234, 2015.
[96] M. A. Hoque, F. M. Hassan, M.-H. Seo, J.-Y. Choi, M. Pritzker, S. Knights, S. Ye, and Z. Chen, "Optimization of sulfur-doped graphene as an emerging platinum nanowires support for oxygen reduction reaction," *Nano Energy*, vol. 19, pp. 27–38, 2016.
[97] Y. Garsany, O. A. Baturina, K. E. Swider-Lyons, and S. S. Kocha, "Experimental methods for quantifying the activity of platinum electrocatalysts for the oxygen reduction reaction.," *Anal. Chem.*, vol. 82, no. 15, pp. 6321–8, Aug. 2010.
[98] A. Pozio, M. De Francesco, A. Cemmi, F. Cardellini, and L. Giorgi, "Comparison of high surface Pt/C catalysts by cyclic voltammetry," *J. Power Sources*, vol. 105, no. 1, pp. 13–19, 2002.
[99] K. R. Cooper, "in Situ Pem Fuel Cell Electrochemical Surface Area and Catalyst Utilization Measurement," *Fuel Cell Mag.*, pp. 1–3, 2009.
[100] K. Shinozaki, J. W. Zack, R. M. Richards, B. S. Pivovar, and S. S. Kocha, "Oxygen Reduction Reaction Measurements on Platinum Electrocatalysts Utilizing Rotating Disk Electrode Technique: I. Impact of Impurities, Measurement Protocols and Applied Corrections," *J. Electrochem. Soc.*, vol. 162, no. 10, pp. F1144–F1158, 2015.
[101] D. C. Higgins, D. Meza, and Z. Chen, "Nitrogen-Doped Carbon Nanotubes as Platinum Catalyst Supports for Oxygen Reduction Reaction in Proton Exchange Membrane Fuel Cells," *J. Phys. Chem. C*, vol. 114, no. 50, pp. 21982–21988, Dec. 2010.
[102] B. Y. Xia, H. Bin Wu, Y. Yan, H. B. Wang, and X. Wang, "One-pot synthesis of platinum nanocubes on reduced graphene oxide with enhanced electrocatalytic activity," *Small*, vol. 10, no. 12, pp. 2336–2339, 2014.
[103] P. Strasser, S. Koh, T. Anniyev, J. Greeley, K. More, C. Yu, Z. Liu, S. Kaya, D. Nordlund, H. Ogasawara, M. F. Toney, and A. Nilsson, "Lattice-strain control of the activity in dealloyed core-shell fuel cell catalysts.," *Nat. Chem.*, vol. 2, no. 6, pp. 454–460, 2010.
[104] V. A. Sethuraman, D. Vairavapandian, M. C. Lafouresse, T. A. Maark, N. Karan, S. Sun, U. Bertocci, A. A. Peterson, G. R. Stafford, and P. R. Guduru, "Role of Elastic Strain on Electrocatalysis of Oxygen Reduction Reaction on Pt," *J. Phys. Chem. C*, vol. 119, no. 33, pp. 19042–19052, 2015.
[105] S. Zhang, X. Zhang, G. Jiang, H. Zhu, S. Guo, D. Su, G. Lu, and S. Sun, "Tuning nanoparticle structure and surface strain for catalysis optimization," *J. Am. Chem. Soc.*, vol. 136, no. 21, pp. 7734–7739, 2014.
[106] S. Guo and S. Sun, "FePt nanoparticles assembled on graphene as enhanced catalyst for oxygen reduction reaction," *J. Am. Chem. Soc.*, vol. 134, no. 5, pp. 2492–2495, 2012.

[107] H. Zhu, S. Zhang, D. Su, G. Jiang, and S. Sun, "Surface Profile Control of FeNiPt/Pt Core/Shell Nanowires for Oxygen Reduction Reaction," *Small*, vol. 11, no. 29, pp. 3545–3549, 2015.
[108] Q. Li, L. Wu, G. Wu, D. Su, H. Lv, S. Zhang, W. Zhu, A. Casimir, H. Zhu, A. Mendoza-Garcia, and S. Sun, "New Approach to Fully Ordered fct-FePt Nanoparticles for Much Enhanced Electrocatalysis in Acid," *Nano Lett.*, vol. 15, no. 4, pp. 2468–2473, 2015.
[109] X. Sun, D. Li, Y. Ding, W. Zhu, S. Guo, Z. L. Wang, and S. Sun, "Core/Shell Au/CuPt Nanoparticles and Their Dual Electrocatalysis for Both Reduction and Oxidation Reactions," *J. Am. Chem. Soc.*, vol. 136, no. 15, pp. 5745–5749, Apr. 2014.
[110] D. C. Higgins, S. Ye, S. Knights, and Z. Chen, "Highly Durable Platinum-Cobalt Nanowires by Microwave Irradiation as Oxygen Reduction Catalyst for PEM Fuel Cell," *Electrochem. Solid-State Lett.*, vol. 15, no. 6, p. B83, 2012.
[111] D. C. Higgins, R. Wang, M. A. Hoque, P. Zamani, S. Abureden, and Z. Chen, "Morphology and composition controlled platinum–cobalt alloy nanowires prepared by electrospinning as oxygen reduction catalyst," *Nano Energy*, vol. 10, pp. 135–143, Nov. 2014.
[112] B. N. Wanjala, B. Fang, S. Shan, V. Petkov, P. Zhu, R. Loukrakpam, Y. Chen, J. Luo, J. Yin, L. Yang, M. Shao, and C. J. Zhong, "Design of ternary nanoalloy catalysts: Effect of nanoscale alloying and structural perfection on electrocatalytic enhancement," *Chem. Mater.*, vol. 24, no. 22, pp. 4283–4293, 2012.
[113] B. Y. Xia, H. Bin Wu, N. Li, Y. Yan, X. W. D. Lou, and X. Wang, "One-Pot Synthesis of Pt-Co Alloy Nanowire Assemblies with Tunable Composition and Enhanced Electrocatalytic Properties," *Angew. Chemie Int. Ed.*, vol. 54, no. 12, pp. 3797–3801, Mar. 2015.
[114] A. Peles, M. Shao, and L. Protsailo, "Pt Monolayer Electrocatalyst for Oxygen Reduction Reaction on Pd-Cu Alloy: First-Principles Investigation," *Catalysts*, vol. 5, no. 3, pp. 1193–1201, Jul. 2015.
[115] S. Il Choi, M. Shao, N. Lu, A. Ruditskiy, H. C. Peng, J. Park, S. Guerrero, J. Wang, M. J. Kim, and Y. Xia, "Synthesis and characterization of Pd@Pt-Ni core-shell octahedra with high activity toward oxygen reduction," *ACS Nano*, vol. 8, no. 10, pp. 10363–10371, 2014.
[116] M. Shao, A. Peles, and J. Odell, "Enhanced oxygen reduction activity of platinum monolayer with a gold interlayer on palladium," *J. Phys. Chem. C*, vol. 118, no. 32, pp. 18505–18509, 2014.
[117] M. Shao, G. He, A. Peles, J. H. Odell, J. Zeng, D. Su, J. Tao, T. Yu, Y. Zhu, and Y. Xia, "Manipulating the oxygen reduction activity of platinum shells with shape-controlled palladium nanocrystal cores.," *Chem. Commun. (Camb).*, vol. 49, no. 79, pp. 9030–2, 2013.
[118] M. P. Humbert, B. H. Smith, Q. Wang, S. N. Ehrlich, and M. Shao, "Synthesis and Characterization of Palladium-Platinum Core-Shell Electrocatalysts for Oxygen Reduction," *Electrocatalysis*, vol. 3, no. 3, pp. 298–303, 2012.
[119] D. F. van der Vliet, C. Wang, D. Tripkovic, D. Strmcnik, X. F. Zhang, M. K. Debe, R. T. Atanasoski, N. M. Markovic, and V. R. Stamenkovic, "Mesostructured thin films as electrocatalysts with tunable composition and surface morphology.," *Nat. Mater.*, vol. 11, no. 12, pp. 1051–8, 2012.
[120] C. Cui, L. Gan, H. H. Li, S. H. Yu, M. Heggen, and P. Strasser, "Octahedral PtNi nanoparticle catalysts: Exceptional oxygen reduction activity by tuning the alloy particle surface composition," *Nano Lett.*, vol. 12, no. 11, pp. 5885–5889, 2012.
[121] S. Zhang, Y. Hao, D. Su, V. V. T. Doan-Nguyen, Y. Wu, J. Li, S. Sun, and C. B. Murray, "Monodisperse core/shell Ni/FePt nanoparticles and their conversion to Ni/Pt to catalyze oxygen reduction," *J. Am. Chem. Soc.*, vol. 136, no. 45, pp. 15921–15924, 2014.
[122] N. Cheng, J. Liu, M. N. Banis, D. Geng, R. Li, S. Ye, S. Knights, and X. Sun, "High stability and activity of Pt electrocatalyst on atomic layer deposited metal oxide/nitrogen-doped graphene hybrid support," *Int. J. Hydrogen Energy*, vol. 39, no. 28, pp. 15967–15974, 2014.
[123] H. N. Yang, D. C. Lee, K. W. Park, and W. J. Kim, "Platinum–boron doped graphene intercalated by carbon black for cathode catalyst in proton exchange membrane fuel cell," *Energy*, vol. 89, pp. 500–510, Sep. 2015.

[124] D. C. Higgins, F. M. Hassan, M. H. Seo, J. Y. Choi, M. A. Hoque, D. U. Lee, and Z. Chen, "Shape-controlled octahedral cobalt disulfide nanoparticles supported on nitrogen and sulfur-doped graphene/carbon nanotube composites for oxygen reduction in acidic electrolyte," *J. Mater. Chem. A*, vol. 3, no. 12, pp. 6340–6350, 2015.
[125] R. Wang, D. C. Higgins, M. A. Hoque, D. Lee, F. Hassan, and Z. Chen, "Controlled Growth of Platinum Nanowire Arrays on Sulfur Doped Graphene as High Performance Electrocatalyst," *Sci. Rep.*, vol. 3, p. 2431, Aug. 2013.
[126] J. Snyder, I. McCue, K. Livi, and J. Erlebacher, "Structure/Processing/Properties Relationships in Nanoporous Nanoparticles As Applied to Catalysis of the Cathodic Oxygen Reduction Reaction," *J. Am. Chem. Soc.*, vol. 134, no. 20, pp. 8633–8645, May 2012.
[127] Z. Chen, M. Waje, W. Li, and Y. Yan, "Supportless Pt and PtPd Nanotubes as Electrocatalysts for Oxygen-Reduction Reactions," *Angew. Chemie Int. Ed.*, vol. 46, no. 22, pp. 4060–4063, May 2007.
[128] A. Holewinski, J.-C. Idrobo, and S. Linic, "High-performance Ag–Co alloy catalysts for electrochemical oxygen reduction," *Nat. Chem.*, vol. 6, no. 9, pp. 828–834, Aug. 2014.
[129] S. Khateeb, S. Guerreo, D. Su, R. M. Darling, L. V. Protsailo, and M. Shao, "Fuel Cell Performance of Palladium-Platinum Core-Shell Electrocatalysts Synthesized in Gram-Scale Batches," *J. Electrochem. Soc.*, vol. 163, no. 7, pp. F708–F713, 2016.
[130] L. Zhang, J. Niu, M. Li, and Z. Xia, "Catalytic mechanisms of sulfur-doped graphene as efficient oxygen reduction reaction catalysts for fuel cells," *J. Phys. Chem. C*, vol. 118, no. 7, pp. 3545–3553, 2014.
[131] J. Liang, Y. Jiao, M. Jaroniec, and S. Z. Qiao, "Sulfur and nitrogen dual-doped mesoporous graphene electrocatalyst for oxygen reduction with synergistically enhanced performance," *Angew. Chemie - Int. Ed.*, vol. 51, no. 46, pp. 11496–11500, 2012.

Appendix

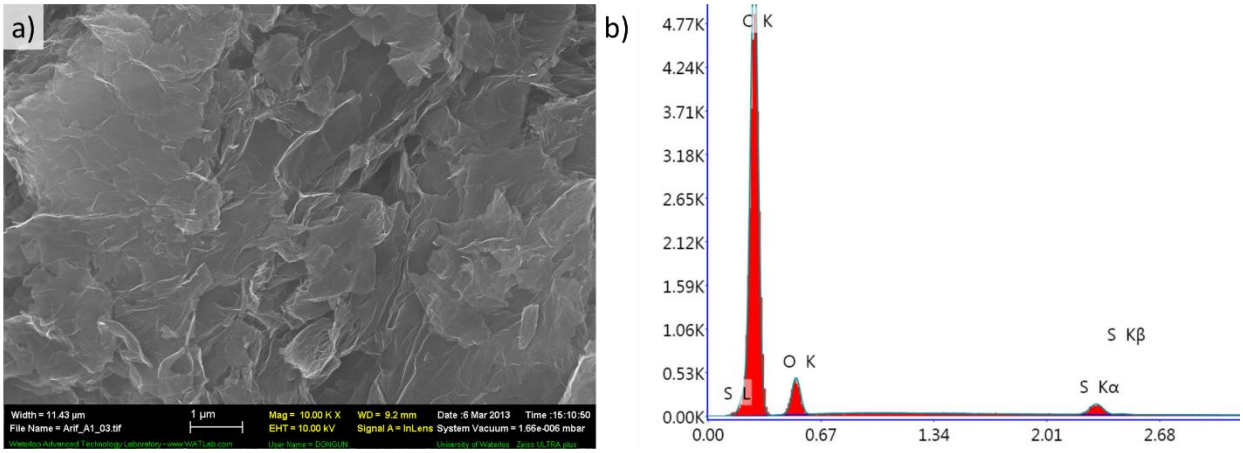

Figure A1: (a) SEM image of SG and (b) EDX of SG.

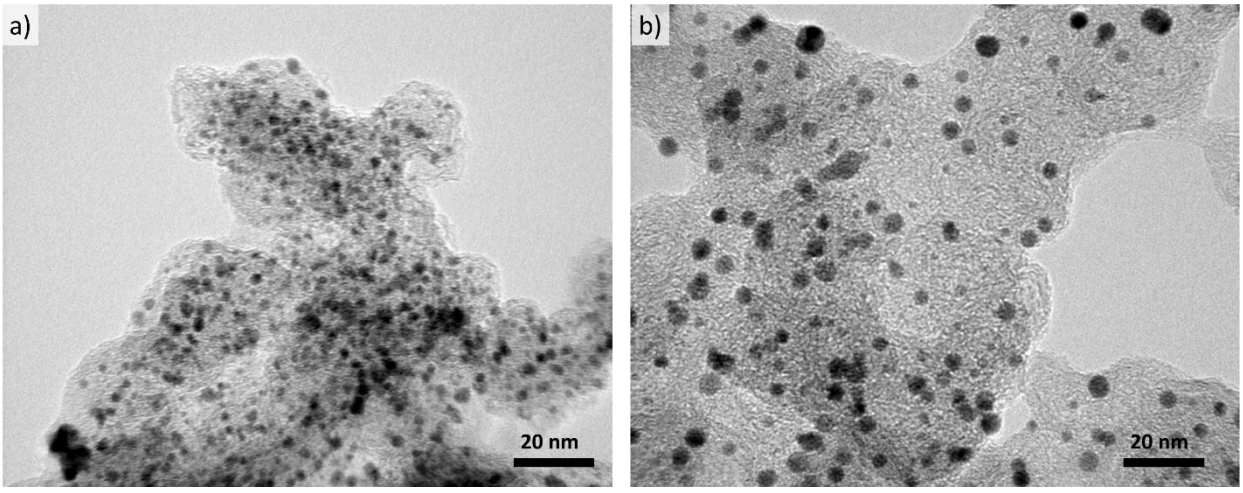

Figure A2. TEM images of Pt/C (a) before ADT and (b) after ADT.

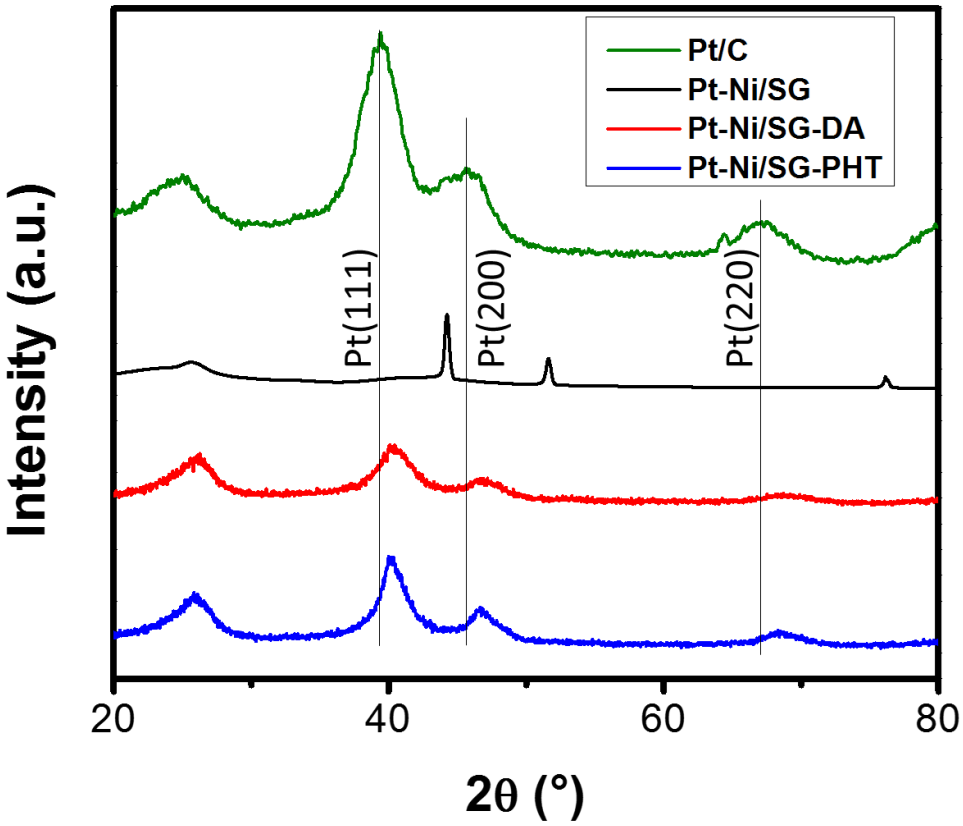

Figure A3. XRD patterns of Pt-Ni/SG, Pt-Ni/SG-DA, Pt-Ni/SG-PHT and commercial Pt/C.

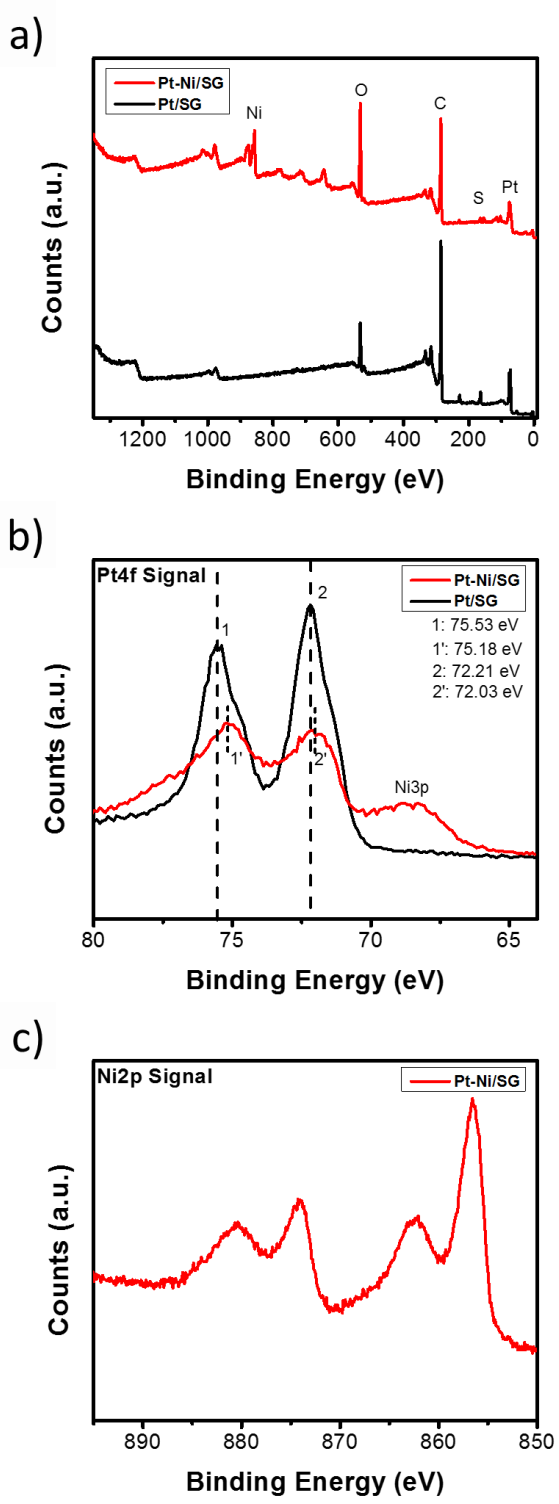

Figure A4. XPS spectra for (a) full range of Pt/SG and Pt-Ni/SG, (b) Pt4f spectra of Pt/SG and Pt-Ni/SG, and (c) Ni2p spectra of Pt-Ni/SG.

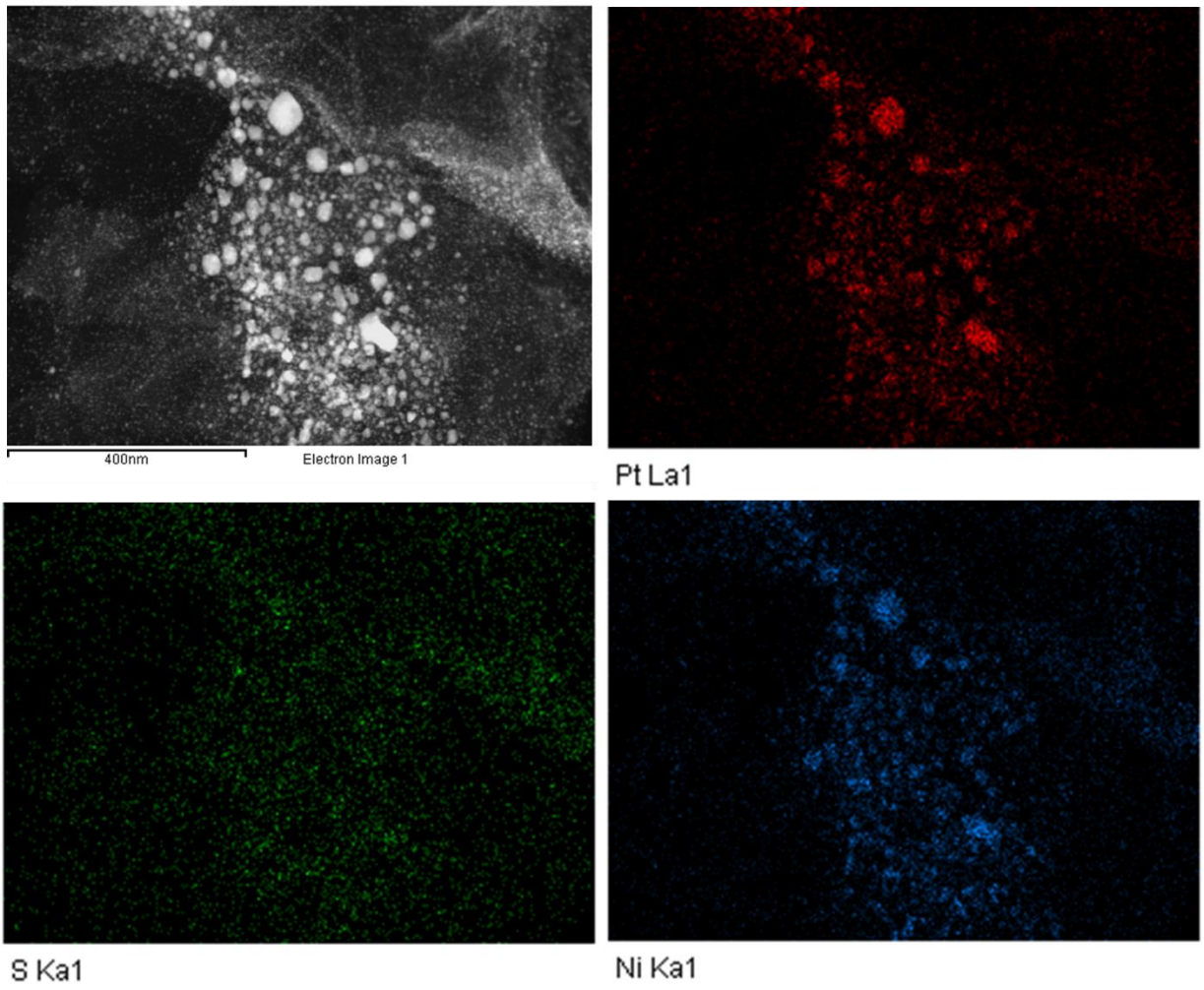

Figure A5. Elemental mapping of Pt-Ni/SG for S, Pt and Ni.

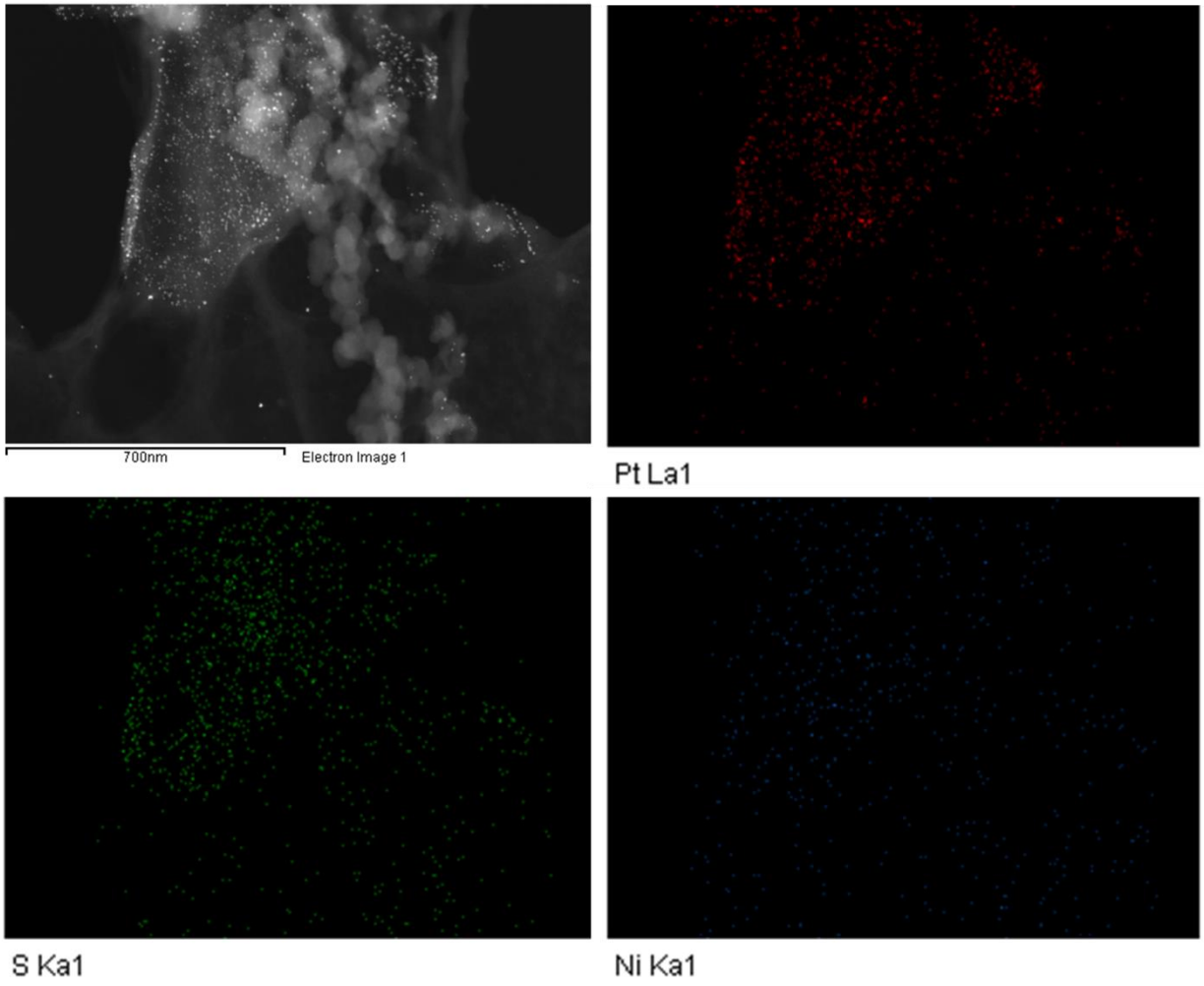

Figure A6. Elemental mapping of Pt-Ni/SG-ADT for S, Pt and Ni.

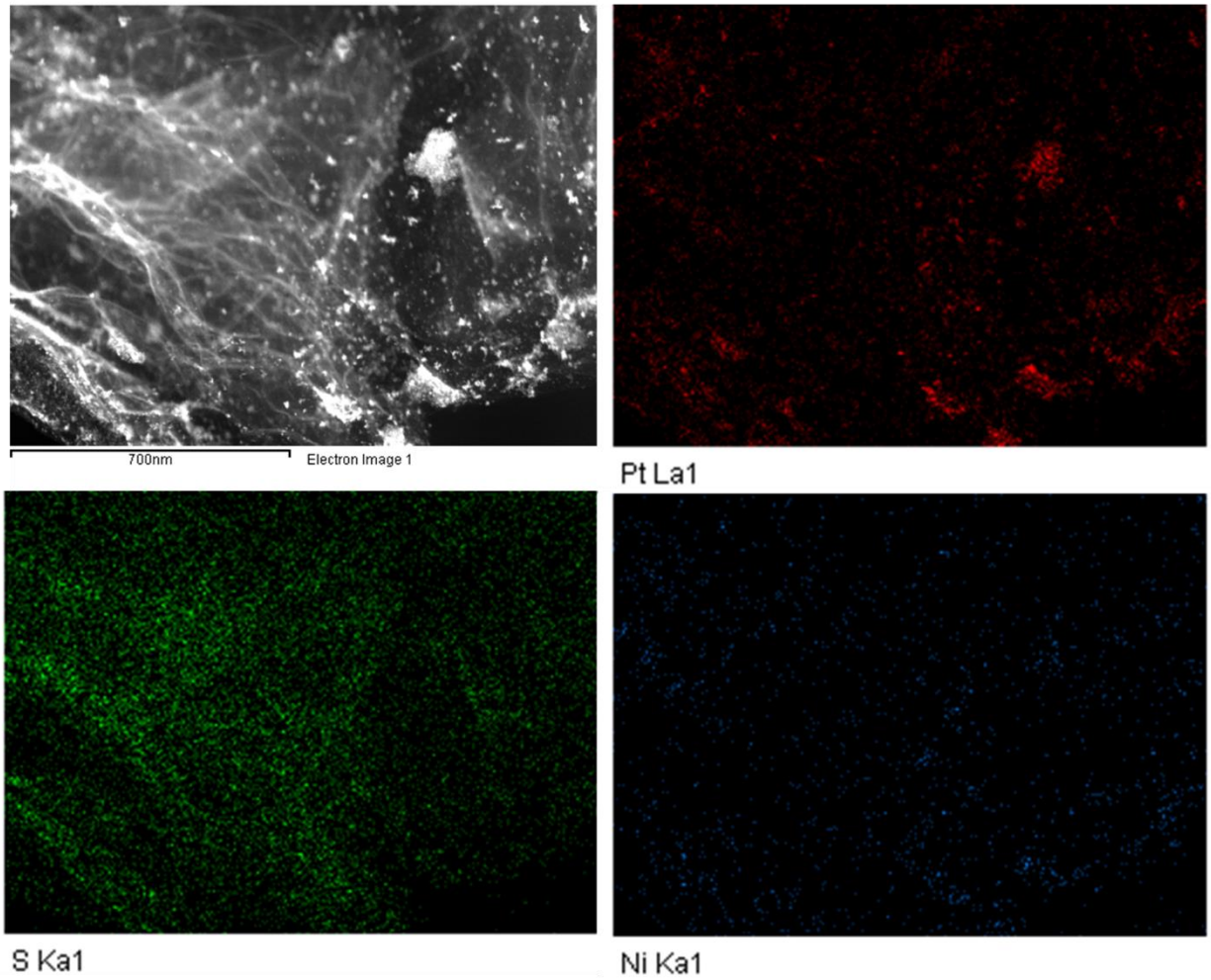

Figure A7. Elemental mapping of Pt-Ni/SG-DA for S, Pt and Ni.

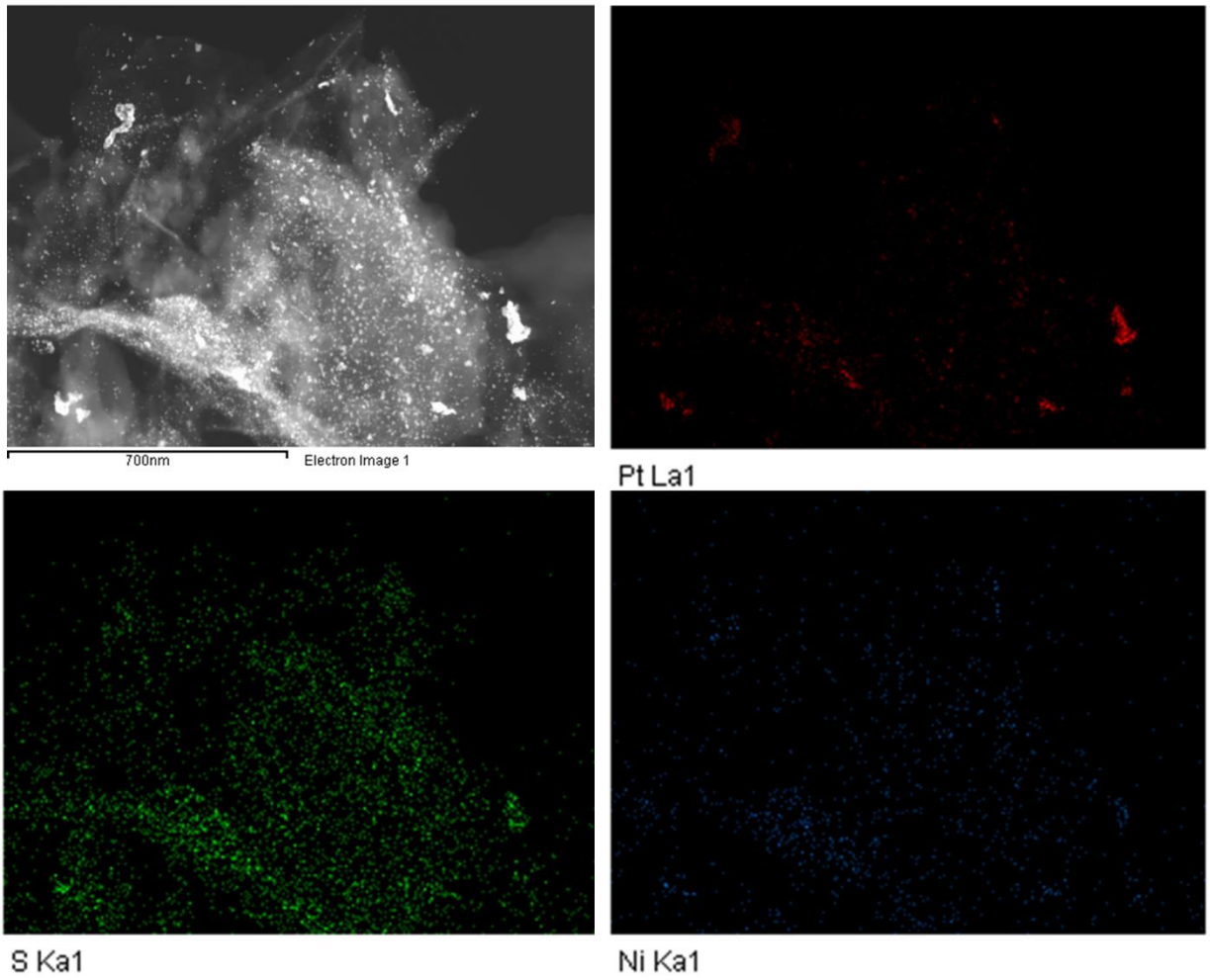

Figure A8. Elemental mapping of Pt-Ni/SG-DA-ADT for S, Pt and Ni.

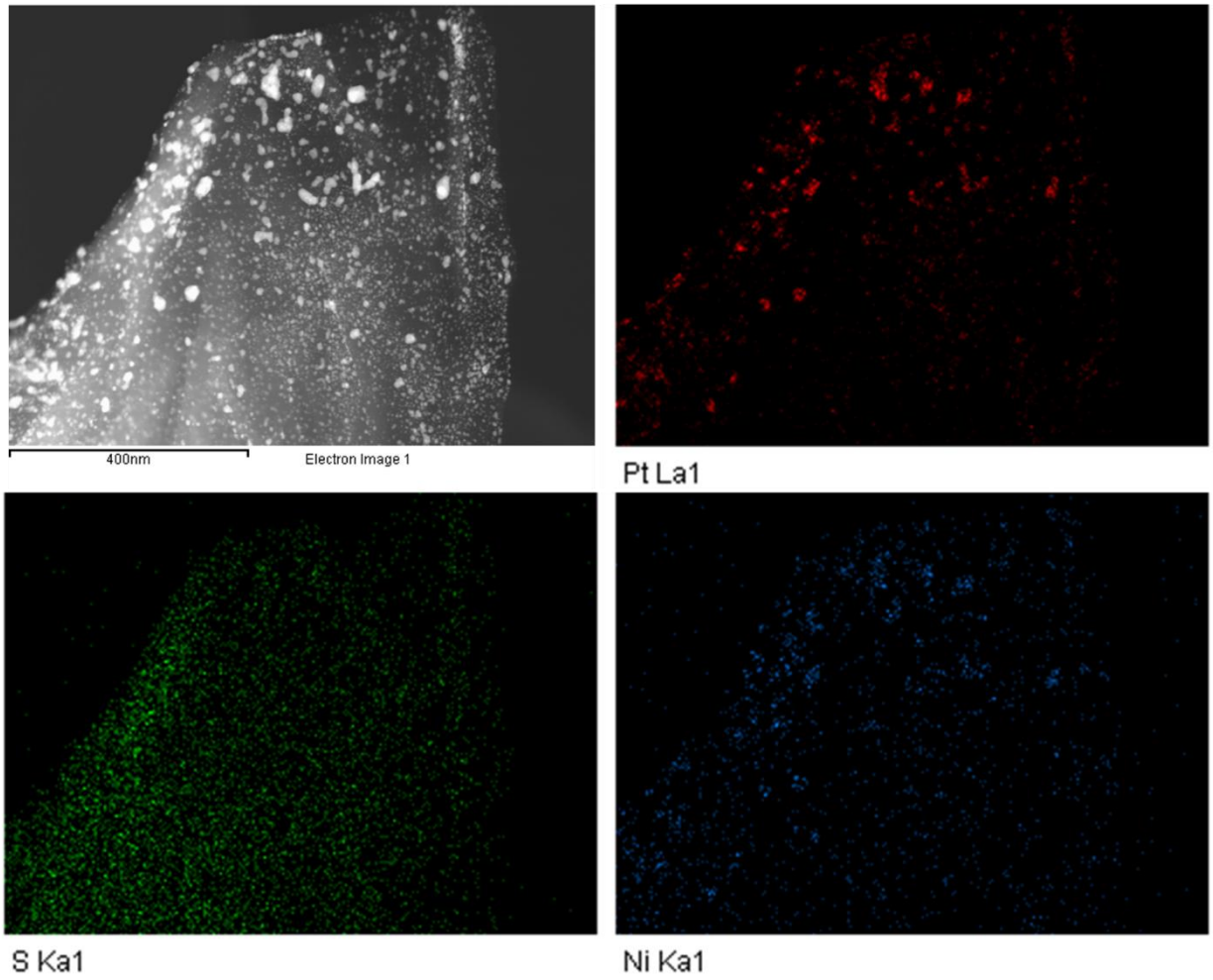

Figure A9. Elemental mapping of Pt-Ni/SG-PHT for S, Pt and Ni.

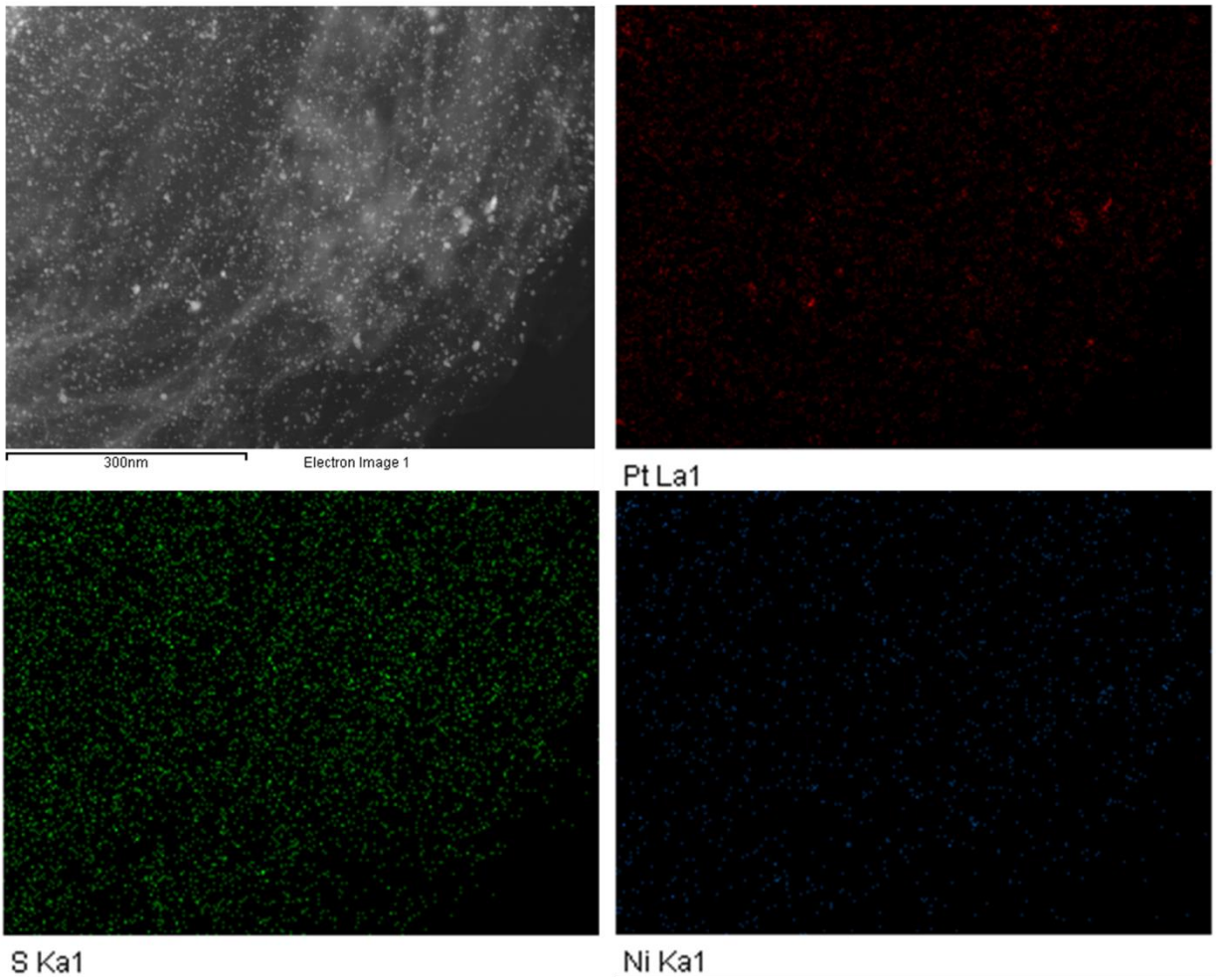

Figure A10. Elemental mapping of Pt-Ni/SG-PHT-ADT for S, Pt and Ni.

Table A2. Metal content of catalysts via ICP.

Catalyst	Nickel Mass %	Platinum Mass %
Pt-Ni/SG	16.78	10.73
Pt-Ni/SG-DA	0.24	10.00
Pt-Ni/SG-PHT	0.29	11.17